J. Fluid Mech. (2019), *vol.* 863, *pp.* 757–788.
doi:10.1017/jfm.2018.1026

Water entry of rounded cylindrical bodies with different aspect ratios and surface conditions

Nayoung Kim[1] **and Hyungmin Park**[1,2,†]

[1]Department of Mechanical and Aerospace Engineering, Seoul National University, Seoul 08826, Korea

[2]Institute of Advanced Machines and Design, Seoul National University, Seoul 08826, Korea

(Received 15 June 2018; revised 9 December 2018; accepted 14 December 2018;
first published online 28 January 2019)

In the present study, we experimentally investigate water surface deformation due to the impact of rounded cylindrical projectiles with different aspect ratios (1.0–8.0). The subsequent jet and splash formation is closely related to the dynamics of an underwater cavity. To control the cavity formation, two kinds of surface conditions (smooth and rough) are applied to the front parts of the projectiles, and two impact speeds are considered. The Froude, Reynolds and Weber numbers are in the ranges of 32–90, 5×10^4–8.4×10^4 and 1700–5000, respectively. When the front is smooth, the water film rises up along the body surface immediately after impact, and the temporal variation of its height is analytically estimated. The film converges at the rear pole to create an apex jet at lower aspect ratios and simply rises up and falls with the body at higher aspect ratios. The jets could be further distinguished as thin and thick jets, whose breakdown is found to be a function of the viscous force and surface tension, i.e. the Ohnesorge number. On the other hand, when the front is rough, the water film cannot rise up along the body surface, and instead early separation occurs to make the splash above a free surface. The splash size is quantified to assess the effects of the aspect ratio and impact speed. Upon splash formation, a cavity is created under the free surface, which emanates from the nose of the projectile. As the body sinks, the cavity pinch-off occurs due to the imbalance between the hydrostatic pressure and air pressure inside the cavity. At higher aspect ratios, cavity pinch-off occurs on the side wall of the projectile and leaves a portion of the cavity bubble on it. When the surface is smooth, no underwater cavity forms. Finally, we compare the hydrodynamic force acting on the sinking bodies with and without cavity formation, based on the underwater trajectory of each projectile. It is found that the underwater cavity reduces the drag force on the sinking body when it fully encapsulates the body; however, if the air bubbles are partially attached to the body after pinch-off, they tend to detach irregularly or impose additional drag on the body.

Key words: multiphase flow, thin films

1. Introduction

The deformation of an interface between two separated fluids (e.g. air and water) by a solid projectile passing through it is a famous classical fluid dynamics problem.

† Email address for correspondence: hminpark@snu.ac.kr

Despite the simple configuration, the subsequent phenomena such as the formation and evolution of a splash, jet and cavity above and below the free surface exhibit complex variations depending on the body geometry, fluid and material properties and impact conditions (Duclaux *et al.* 2007; Duez *et al.* 2007; Aristoff & Bush 2009; Truscott, Epps & Techet 2012; Truscott, Epps & Belden 2014). These variations are important because the unsteady dynamics of these interfacial features is closely related to changes in the hydrodynamic loading of the projectile. For example, Truscott *et al.* (2012) studied a sphere descending underwater and showed that the pressure near the front stagnation position dominates the flow around the sphere when there is a cavity, while the case without a cavity is affected by the added mass, buoyancy and wake defect. Water entry has also been investigated as a simplified problem to understand the underlying physics of ship slamming (Zhao & Faltinsen 1993), air-to-seawater ballistics for military applications (May 1952; Yao *et al.* 2014), the stability of offshore structures (Sun & Faltinsen 2006), sports engineering topics such as diving and rowing (Harrison *et al.* 2016), stone skipping (Clanet, Hersen & Bocquet 2004; Rosellini *et al.* 2005), film coating in chemical processes (Benkreira & Khan 2008) and so on. Recently, regarding the role of a cavity, the flow condition for a near-zero drag projectile has been investigated as well (Vakarelski *et al.* 2017).

As reviewed by Truscott *et al.* (2014), the general picture of free-surface deformation due to an impacting body involves the unsteady processes of a splash, cavity and jet flow. For example, as a sphere enters water with cavity formation, a jet is first ejected in the radial direction above the free surface, and a splash is then formed. When the Weber number is sufficiently high, the splash converges into a dome (Aristoff & Bush 2009; Marston *et al.* 2016). Below the free surface, the cavity pinches off due to the hydrostatic pressure (called a deep seal), and the dome comes down to the free surface to prevent further cavity expansion (surface seal). While the deep seal occurs near the midpoint between the free surface and the body, the pinch-off occurring close to the free surface is called a shallow seal. When the pinch-off occurs close to the body, leaving almost no cavity bubble attached to the body, it is classified as a quasi-static seal (Aristoff & Bush 2009). When the sphere enters a free surface without forming a cavity, a thin jet is induced above the free surface instead of a splash. Although this interesting phenomenon was reported a long time ago (Worthington 1908), recent advances in high-speed imaging have spurred the accumulation of relevant data and theoretical analysis in the past decade (Lee, Longoria & Wilson 1997; Duclaux *et al.* 2007; Aristoff & Bush 2009; Aristoff *et al.* 2010; Truscott *et al.* 2012).

The entry of a solid object (characteristic size R and downward impact speed of $U_\circ$ at the interface) into a liquid is affected by the surface tension, fluid properties (density and viscosity), solid properties (density), surface conditions of the object (roughness and wettability) and gravity. Thus, it is possible to characterize the qualitative picture of a water entry with dimensionless parameters such as the Froude number ($Fr = U_\circ^2/gR$), Reynolds number ($Re = \rho U_\circ R/\mu$), Weber number ($We = \rho U_\circ^2 R/\sigma$), Bond number ($Bo = \rho g R^2/\sigma$), capillary number ($Ca = \mu U_\circ/\sigma$) and solid–liquid density ratio ($d = \rho_s/\rho$). Here, σ is the surface tension, μ and ρ are the dynamic viscosity and density of the liquid, respectively, ρ_s is the solid density and g is the gravitational acceleration. For example, Thoroddsen *et al.* (2004) experimentally demonstrated that a radial jet appears approximately 8 μs after a sphere first contacts a free surface at $Re \simeq 10^5$ and that its velocity is proportional to $U_\circ^{0.5}$. Marston, Vakarelski & Thoroddsen (2011) observed that air is trapped between the free surface and front part of a sphere at the instant of impact (when $We > 1$) and

shrinks from a sheet to a bubble as the sphere descends at $Ca < 1$ and $Re > 1000$. Marston *et al.* (2016) showed that surface tension plays an important role along with pressure at the moment of splash closing. While the splash width increases as the air pressure decreases during splash growth, the rate of collapse later is more influenced by surface tension for $We = \boldsymbol{O}(10^3–10^5)$ and $Re = \boldsymbol{O}(10^4–10^5)$. Below the free surface, a cavity is formed when the capillary number (Ca) exceeds a critical value (Dussan 1979; Duez *et al.* 2007) and pinches off due to the hydrostatic pressure. Mansoor *et al.* (2014) found that a deep seal occurs before a surface seal or is reversed depending on Fr. With a surface seal, the ratio between the distances from the free surface to the pinch-off location (H_p) and the impacting sphere centre (H) decreases with increasing Fr (when $Fr > 100$). By varying the density of a falling sphere, Aristoff *et al.* (2010) showed that the cavity pinch-off position and time (t_p) increase linearly with Fr, while H_p/H remains almost constant when the momentum loss of the impacting sphere is small. This behaviour agrees with the results obtained by Duclaux *et al.* (2007), who found that H_p/H is constant at 0.5 when $Fr < 1000$. The larger Fr is, the larger the volume of air is that is attached to the sphere after pinch-off. When the water entry of a projectile does not involve cavity formation, a thin liquid film moves up along the sphere surface after impact, which is followed by a jet flow rising in two steps from the top of the sphere (Kuwabara, Tanba & Kono 1987). The dimensionless initial velocities of the first and second jet flows are approximately constant irrespective of the Re of $\boldsymbol{O}(10^4)$. Kubota & Mochizuki (2009) reported that the larger We is, the more the liquid film (jet) is broken into droplets.

In addition, the body surface condition can change the global picture of water entry. For example, the static contact angle (θ_c) is known to be an important parameter in defining surface wettability. Duez *et al.* (2007) explained that the minimum impact velocity required to form a cavity is proportional to the capillary velocity, which is the ratio of surface tension to liquid viscosity. The critical velocity of an impacting sphere with a hydrophilic surface ($\theta_c < 90°$) is proportional to the capillary velocity, while that of a sphere with a hydrophobic surface ($\theta_c > 90°$) is proportional to θ_c^3 as well as the capillary velocity. Therefore, a hydrophobic sphere creates a cavity even at a relatively low impact velocity. Although it has not been investigated in detail, even slight surface contamination (i.e. roughness) would also lead to cavity formation behind a submerging body under conditions where the smooth counterpart would not (Worthington 1908; May 1951; Grumstrup, Keller & Belmonte 2007; Zhao, Chen & Wang 2014).

It is clear that our knowledge about the solid–fluid interactions occurring at free surfaces has increased significantly. However, most previous studies have considered the entry of spheres, and it is necessary to extend our understanding to different shapes. For example, an elongated cylindrical projectile (of length L) is more closely connected to practical applications such as expendable bathythermographs and naval weapons. Actually, some studies have focused on the entry of non-spherical impacting bodies. Bodily, Carlson & Truscott (2014) conducted experiments with a long axisymmetric body (aspect ratio, $AR = L/(2R) = 10$) with $Fr = 56–80$, $Re = 3.4–4.0 \times 10^4$ and $We = 1235–1710$ and observed how the entry angle, nose shape and position of the centre of mass affect its trajectory after impact. They showed that the projectile moves in the lateral direction as the entry angle increases (i.e. it deviates more from the vertical axis), the nose shape becomes conical, and the centre of mass moves farther from the nose. Cavity pinch-off occurs twice: first at the side of the body and then in the wake. Gekle *et al.* (2008) showed that the location of cavity pinch-off behind a cylinder ($AR = 3.7$) is not linearly proportional

to Fr, unlike in the case of a sphere. Aristoff & Bush (2009) demonstrated that the cavity behind a long cylinder ($AR = 75$) is formed in a narrow region behind the tail. Yao *et al.* (2014) tried to predict the trajectory and cavity shape of a bullet-shaped projectile ($AR = 5.7$, $Re = 1.3 \times 10^5$ and $Fr = 2600$) using a theoretical approach (Duclaux *et al.* 2007; Aristoff & Bush 2009), and showed that their predictions agree with the experimental results before cavity pinch-off occurs.

Thus, it is necessary to study free-surface deformation occurring upon the entry of a cylindrical body in more detail. In particular, it is of great interest to examine the effects of the projectile AR in the cases with and without cavity formation. In the present study, we experimentally investigate the vertical free fall of a slender solid body (whose nose and tail parts have hemispherical shapes) onto an air–water interface. We focus on measuring the morphing of the free surface into a jet/splash and an underwater cavity via high-speed imaging. AR is varied from 1.0 (sphere) to 8.0. The non-dimensional variables are $Fr = 32$–90, $Re = 5$–8.4×10^4, $We = 1700$–5000, $Bo = 55$ and $Ca = 0.03$–0.06, for which no cavity would be formed by the water entry of a hydrophilic object. Since cavity formation and growth are of great interest, we also test the cavity-forming case by roughening the nose part of each projectile. To the best of our knowledge, this is the first study in which the effects of the AR of a projectile on water entry have been systematically investigated, comparing the cases with and without cavity formation.

The paper is organized as follows. In § 2, we explain the experimental set-up, including the high-speed imaging technique, and characterize the considered impacting bodies. The water entry of a projectile with a smooth surface (without a cavity) is discussed in § 3. In § 4, we address the case with a roughened surface (with a cavity). In § 5, we further examine the effects of a cavity on the hydrodynamic force acting on a sinking body. A summary and the conclusions are given in § 6.

2. Experimental set-up and procedures

In the present study, the water entry of a cylindrical body is measured in a large acrylic tank ($800 \times 800 \times 1000$ mm^3) filled with tap water (static), as shown in figure 1(*a*). The projectiles (made of acrylic) have the form of spheres extended along the longitudinal direction (length L); i.e. both the nose and tail parts are hemispherical (radius $R = 0.5D = 20$ mm) and AR ($= L/D$) is set to 1.0 (sphere), 2.0, 4.0 and 8.0 (figure 1*b*). Thus, the ratio of body diameter (D) to tank width is $D/D_{tank} = 0.05$, which satisfies the criterion of $D/D_{tank} < 0.075$, at which the tank side walls negligibly affect the measurements according to Mansoor *et al.* (2014). The solid-to-liquid density ratio ($d = \rho_s/\rho$) is approximately 1.2.

To control the cavity formation, we roughened the nose (front hemispherical part) of each projectile with sandpaper (grit number 60). Previously, Zhao *et al.* (2014) showed that the critical impact velocity for cavity formation dramatically decreases when the surface of an impacting body is rough. Scanning electron microscopy (SEM) images of smooth and rough surfaces were taken (see the insets in figure 1*b*) and conventional binarization (Otsu 1979) was applied to quantify the roughness. We calculated the mean roughness (R_a), which is defined as the sum of the vertical deviations divided by the sample length, and was equal to 0.26 μm and 12.98 μm for the smooth and rough surfaces, respectively. In total, eight different projectiles were tested (figure 1*b*). To achieve the free fall of each projectile, it was first attached to an in-house vacuum release system, which was positioned directly above the centre of the water tank. The set-up was designed such that the release height could be adjusted to change the

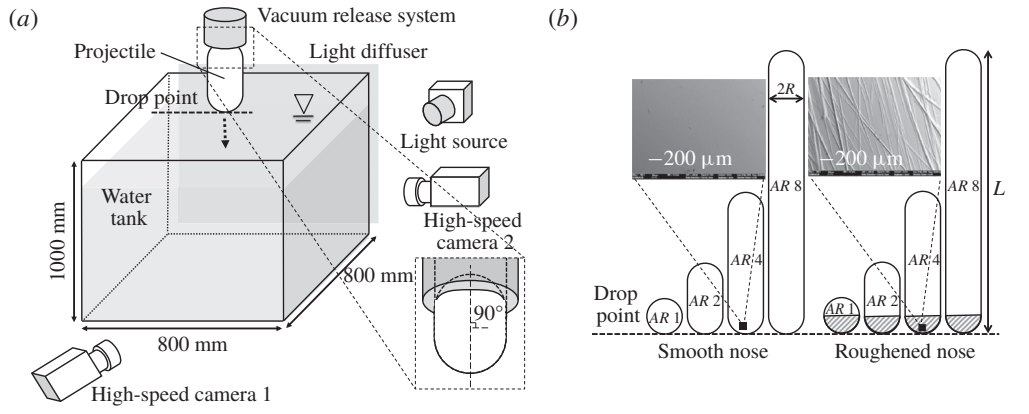

FIGURE 1. (Colour online) (*a*) Experimental set-up for measuring the water entry of a projectile via high-speed imaging. (*b*) Geometry of the projectiles used in the present study. *AR* is varied as 1.0, 2.0, 4.0 and 8.0, and two types of surfaces (smooth and rough) are used for the nose part. In (*b*), the insets are the scanning electron microscopy (SEM) images of the smooth and rough surfaces.

$U_\circ$ (m s^{-1})	*Fr*	*Re* ($\times 10^4$)	*We*	*Bo*	*Ca*
2.5	32	5.0	1736	55	0.0345
4.2	90	8.4	4900	55	0.0579

TABLE 1. Dimensionless variables corresponding to tested conditions. The experiments are conducted with tap water ($\rho = 1000$ kg m^{-3}, $\sigma = 0.0725$ N m^{-1}, $\nu = 10^{-6}$ m^2 s^{-1} and $\mu = 0.001$ N s m^{-2}) and $g = 9.81$ m s^{-2}.

impact speed at the free surface. To guarantee the vertical fall of each body, a hollow cylinder (supporting jig) with an inner diameter equal to the projectile size was fitted on the outer surface of the projectile (see figure 1*a* for details) when it was held by a vacuum pump (Rocker 300, Rocker) that could de-pressurize below 90 kPa (∼90 % of atmospheric pressure). Before release, the jig was adjusted to align the projectile normal to the water surface; the jig was removed before release so as not to interfere with the falling projectile. During the measurements, it was also visually confirmed that the major axis of the projectile was normal to the water surface at the instant of impact (deviation within 0.53° from the vertical axis). For each projectile, the vertical position of the drop point was matched with the front stagnation point (figure 1) such that the nose tip travelled the same distance before impact, regardless of *AR*. In addition to *AR*, we also varied the impact speed ($U_\circ$), setting it equal to 2.5 and 4.2 m s^{-1}. The corresponding non-dimensional variables are summarized in table 1.

To measure the free-surface deformation, we used one or two high-speed cameras (SpeedSense M310, Dantec Dynamics) that could capture images at 3200 f.p.s. (1280 pixel × 800 pixel) and 10 000 f.p.s. (560 pixel × 448 pixel). Tungsten lamps (Openface 750W, ARRI) were used as light sources. The camera, equipped with a 105 mm lens (Nikon), was moved in the vertical direction to measure the flow structures above and below the water surface. To obtain statistically meaningful data, more than 10 independent measurements were performed and analysed for each projectile. The temperature in the laboratory was maintained at approximately 25 °C,

and a break of more than 30 min was included between individual measurements to avoid any disturbance from the previous measurement. With the present set-up, the spatial and temporal resolutions of the measurements were $0.005D$ and $0.03D/U_\circ$, respectively, which are believed to be sufficient to capture the phenomena. Once the high-speed images of the deformed free surface were obtained, they were processed further to detect and track their profiles. We used Matlab code written in-house to obtain the statistical data from the raw images. If necessary, image filters embedded in Matlab, such as a Wiener filter, were used to enhance the signal-to-noise ratio of the data. To track the trajectory of each descending body, we used a Hough function to detect the centre of a sphere ($AR = 1$). For $AR > 1$, we tracked the midpoints of the centres of the hemispherical head and tail parts of the projectile.

To support our analysis, if necessary, we measured the velocity field in the gas (air) and liquid (water) phases induced by the entry of the projectile, via high-speed particle image velocimetry. A green laser sheet (532 nm wavelength) from a continuous-wave laser (RayPower 5000, Dantec Dynamics) illuminated the region around the falling body. As tracers, we used 10 μm-sized hollow glass spheres (110P8, Potters Industries Inc.) for the liquid phase and oil droplets (approximately 1 μm in size) produced by a fog generator (Safex, Dantec Dynamics) for the gas phase. While evaluating the velocity field, a moving mask was applied to the area occupied by the falling body. The raw image was first binarized to eliminate the particle images, thereby highlighting the outer profile of the projectile. Then, the data obtained by applying cross-correlation to the raw particle image were masked. In taking particle images for the gas phase, the pixel intensity of the falling object differed noticeably from that of the background, but the splash could distort the particle images captured through the liquid sheet. Therefore, the splash was masked in the same way as done for the moving projectile. Spurious vectors were replaced by interpolation via the Gaussian weight kernel method (Agüí & Jiménez 1987; Landreth & Adrian 1990). The spatial resolution of the velocity measurements was approximately $0.025D$.

3. Water entry of a projectile without a cavity

3.1. *Overall description of the free-surface deformation*

Figures 2 and 3 show the overall flow structures above and below the free surface, induced by the water entry of a projectile (smooth surface) with different AR, impacting at $U_\circ = 2.5$ m s^{-1} and 4.2 m s^{-1}, respectively (see also supplementary movie S1 available at https://doi.org/10.1017/jfm.2018.1026). Since the smooth acrylic surface had a static contact angle smaller than 90° and the capillary number was less than 0.1, the typical low-speed cavity whose boundary is attached to the nose of the body is not observable (Truscott *et al.* 2014). Rather than a splash accompanied by a cavity, jet flow is evident above the free surface. For the cases of AR 1–4 (at both $U_\circ = 2.5$ and 4.2 m s^{-1}), a vertical jet appears immediately after the projectile is fully submerged (e.g. at $t^* = 2.0$ in figures 2*b* and 3*b*), which breaks up into small droplets later. Here, the dimensionless time is defined as $t^* = tU_\circ/D$ and the instant of impact is set to $t = 0$. As the jet falls, the free surface slightly sags, which is clearer for the higher $U_\circ$ of 4.2 m s^{-1} (at $t^* = 25.0$ in figure 3*b*), in which case the contribution of inertia is greater. As AR increases, the maximum jet height tends to decrease, except when $AR = 8.0$. As shown in figure 2(*d*), the water film that rises along the surface of the projectile (AR 8) does not converge to form a jet, but rather descends together with the body. As the body passes the free surface, it is dragged further downward due to surface tension to form a shallow cavity in the wake behind

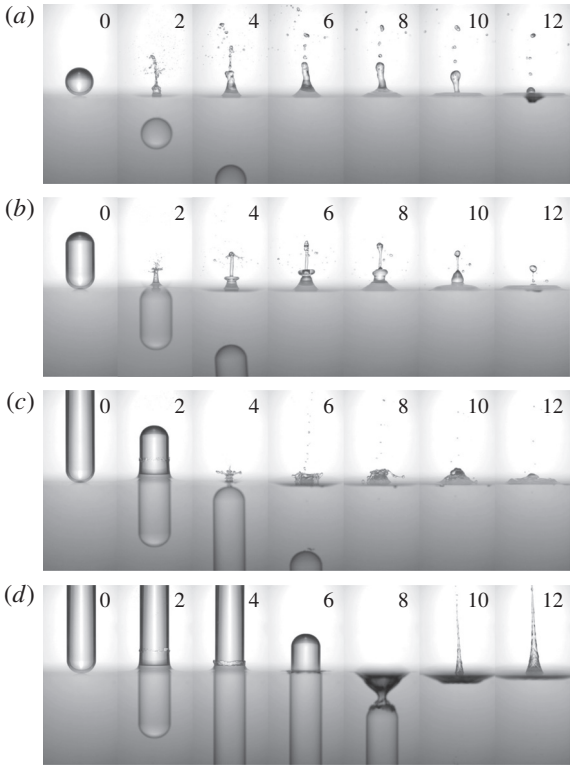

FIGURE 2. Free-surface deformation by the water entry of a body with a smooth surface at $U_\circ = 2.5$ m s^{-1}: (*a*) $AR = 1.0$, (*b*) 2.0, (*c*) 4.0, (*d*) 8.0. The numbers in each image denote the dimensionless time ($t^* = tU_\circ/D$) elapsed after impact ($t = 0$).

the projectile ($t^* = 8.0$ in figure 2*d*). This behaviour is consistent with the description provided by Aristoff & Bush (2009), who explained that the free surface is attached to the rear edge of a cylinder as it enters water and is pulled down to form a cavity. The radial size of this cavity is similar to the cylinder diameter, and cavity pinch-off occurs when the cylinder base reaches a depth equal to the capillary length. This type of cavity is called a quasi-static cavity and has quite low air entrainment. Quasi-static cavities are not created until the tail of the body is fully submerged and are different from those formed by the entry of a body with a roughened front part, as we will discuss in § 4. After the shallow cavity detaches from the body tail, a long jet is induced due to the high pressure in the collapsing cavity ($t^* = 10.0$ in figure 2*d*). Thus, this jet has a different origin from those appearing at smaller *AR*. When $U_\circ = 4.2$ m s^{-1}, the same flow structures (jet and quasi-static cavity) are induced but the cavity shape for *AR* 8 is more distorted due to the increased inertia (after the collapse, most of the cavity bubble descends with the body being attached to it) and thus the jet induced by the collapsing cavity is not well established and becomes shorter (figure 3*d*).

Figure 4 shows the sequence of jet formation for the cases of *AR* 1–4 and demonstrates that jet formation can be understood as a two-step process, i.e. the formation of thin and thick jets. This behaviour is clearly visible for the cases with *AR* 1–2 at $U_\circ = 2.5$ m s^{-1} (figure 4*a*,*b*), and the *AR* 4 case shows a more complex

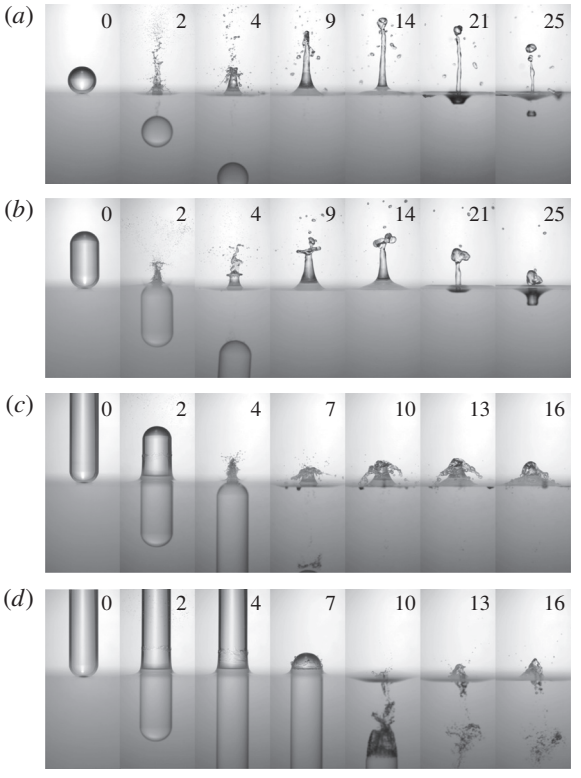

FIGURE 3. Free-surface deformation by the water entry of a body with a smooth surface at $U_\circ = 4.2$ m s^{-1}: (*a*) $AR = 1.0$, (*b*) 2.0, (*c*) 4.0, (*d*) 8.0. The numbers in each image denote t^*.

jet (breakdown into crown-like droplets and another jet due to the collapse of a shallow cavity) (figure 4*c*). The formation of thin and thick jets in the water entry of a sphere was previously mentioned by Kuwabara *et al.* (1987) and is similar to the behaviour occurring in granular impacts (Marston *et al.* 2008; Royer *et al.* 2008) and laser-induced jets (Chen *et al.* 2013), but their mechanisms have not been addressed in detail. Figure 5 illustrates the sequential process of thin and thick jet formation. As we will explain in § 3.2, the water film first rises along the body surface after impact and converges at the rear pole to form a thin jet. As the body sinks, the surrounding water is pushed and dragged around the body tail to induce a stagnation point below the free surface. From this stagnation point, vertical flow is generated and the upward component forms a thick jet over the free surface (§ 3.3).

3.2. *Water film rise and thin jet formation*

Figure 6 shows the sequential movement of a thin water film along the smooth surface of a projectile with different AR at $U_\circ = 2.5$ m s^{-1}. For AR 1, the ascending film gathers at the rear pole and forms a thin, long jet over the free surface (figure 6*a*), which will be referred to as a thin jet. Similar apex jet formation upon the impact of a viscous glycerin droplet onto a lower viscosity liquid was reported previously by Marston & Thoroddsen (2008). They explained that the impact speed directly determines the rise speed of a liquid film and it should be sufficiently fast to give

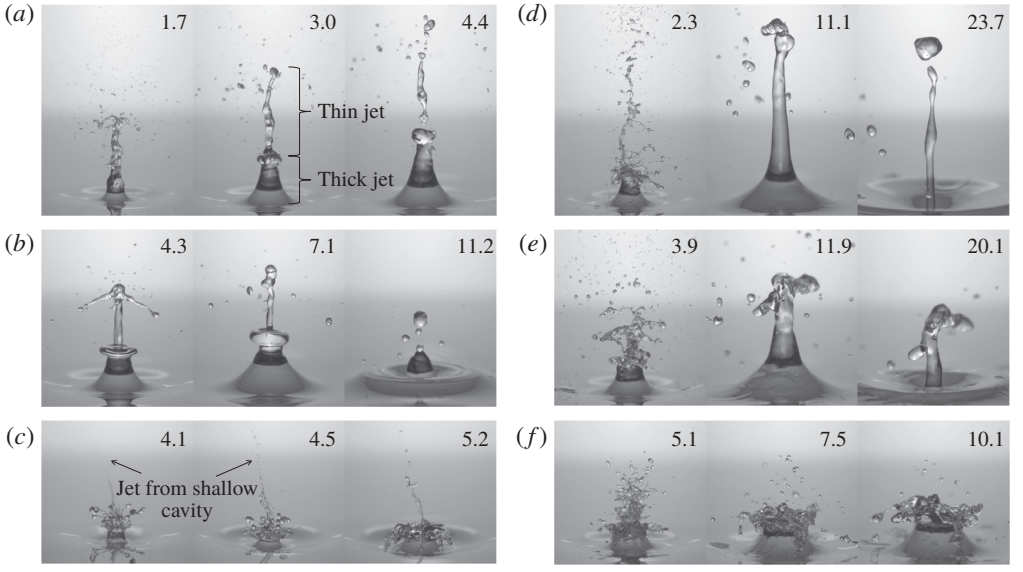

FIGURE 4. Jet formation by the water entry of a body with a smooth surface at $U_\circ = 2.5$ m s^{-1} (*a–c*) and 4.2 m s^{-1} (*d–f*): (*a*,*d*) $AR = 1.0$, (*b*,*e*) 2.0, (*c*,*f*) 4.0. The numbers in each image denote t^*.

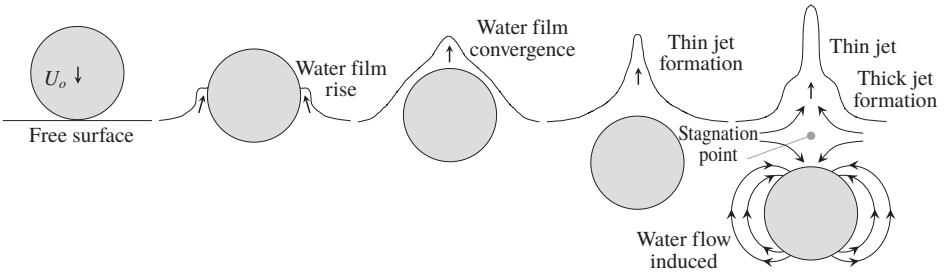

FIGURE 5. Formation of thin and thick jets due to the water entry of a body with a smooth surface.

momentum to the liquid film to ascend to the pole, but not so much as to cause separation from the surface. When $AR = 2.0$, the water film still receives enough momentum to meet at the rear pole and generate a thin jet before the projectile fully submerges (figure 6*b*). The time taken for jet formation increases as AR increases, because it takes longer for the projectile to submerge. When AR increases to 4.0, the water film rises along the side wall of the projectile, stays at a constant height for some time and then falls together with the body (figure 6*c*). In this case, the convergence of the water film is delayed. Since the water film cannot meet at the apex of the projectile, the thin jet formation is not as organized as in the cases of AR 1–2, but the water film breaks into a finger-like shape ($t^* = 3.6$ in figure 6*c*). Below the free surface, a shallow (quasi-static) cavity is formed, and its collapse induces another jet emerging through the water fingers (figure 4*c*). For the highest AR of 8.0, similar to the case of AR 4, the water film stays at a constant height but falls into the free surface before the projectile submerges completely (figure 6*d*). Thus, it is understood

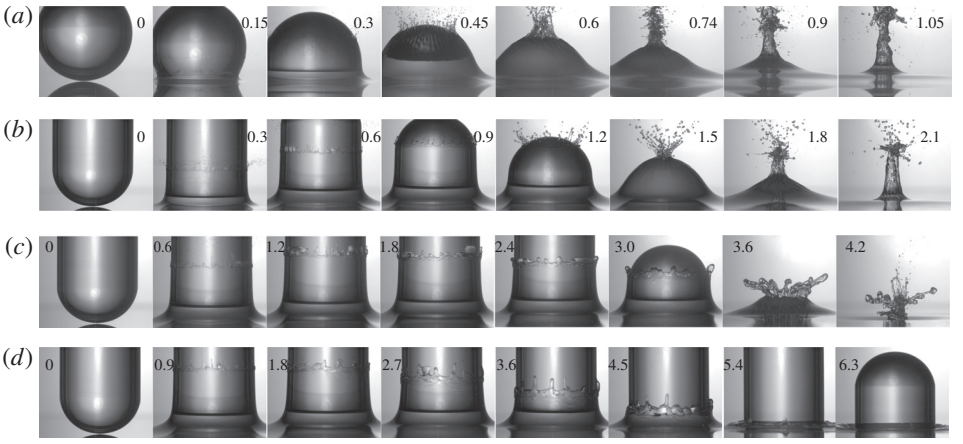

FIGURE 6. Movement of a thin water film along the body surface (smooth) after impact ($U_\circ = 2.5$ m s^{-1}): (*a*) *AR* 1; (*b*) *AR* 2; (*c*) *AR* 4; (*d*) *AR* 8. The numbers in each image denote t^*.

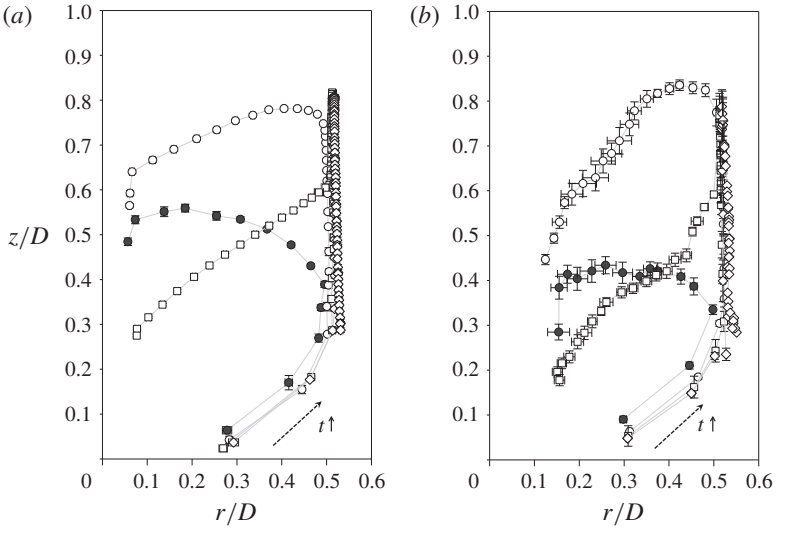

FIGURE 7. Temporal variation of the position of the end of a water film: (*a*) $U_\circ = 2.5$ m s^{-1}; (*b*) 4.2 m s^{-1}. ●, *AR* 1; ○, *AR* 2; □, *AR* 4; ◇, *AR* 8. The origin is defined as the location on the undisturbed free surface that the nose of the body first contacts, and the data are plotted with a time interval Δt^* of 0.05.

that at higher $AR\,(> 4.0)$, the water film does not fully converge at the pole, leaving a sagging space (i.e. cavity) under the free surface.

Figure 7 tracks the end of a water film (i.e. three-phase contact point) while rising along the body surface. Here, r and z denote the radial and vertical directions, respectively, and the origin is defined as the point on the undisturbed free surface that the nose of the body first contacts. The raw images were binarized (Otsu 1979) to distinguish the interfaces between the ambient air, water film and solid surface before measuring the position of the water film. For both $U_\circ = 2.5$ and 4.2 m s^{-1},

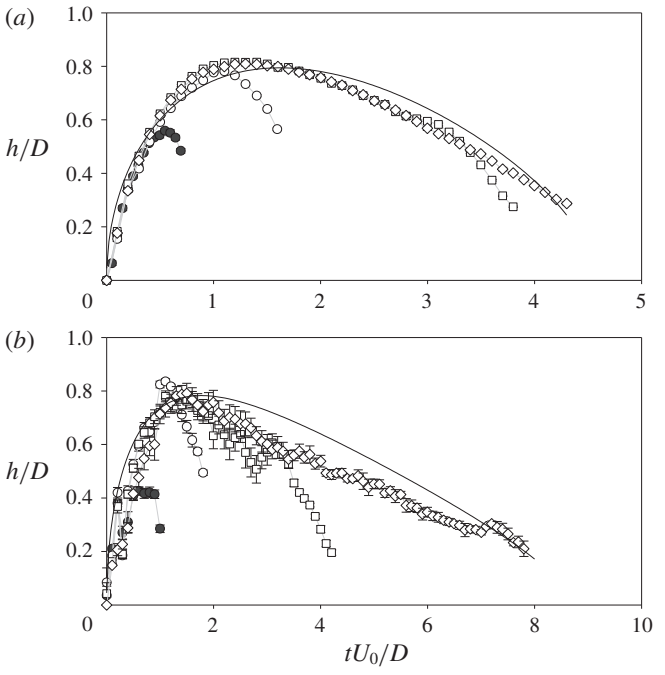

FIGURE 8. Temporal variation of the liquid film height ($h^* = h/D$) from the free surface: (*a*) $U_\circ = 2.5$ m s^{-1}; (*b*) 4.2 m s^{-1}. ●, *AR* 1; ○, *AR* 2; □, *AR* 4; ◇, *AR* 8. The solid lines denote the present estimates (for *AR* 8) (see figure 9 and (3.5)).

the water film follows the surface of the falling projectile and converges near the rear pole ($z/D \simeq 0.5$) for the cases of *AR* 1–2. For *AR* 4, the last location of the film end is around $z/D = 0.2$–0.3, which corresponds to the root of a finger-like jet ($t^* = 3.6$ in figure 6*c*). Thus, the complete convergence of the water film as a jet is not achieved before the body submerges. The water film rises and then simply falls down vertically, for the case of *AR* 8. The initial speed of the water film is not affected much by variations of *AR* and $U_\circ$, but its descending speed later changes considerably (figure 7). In addition, the maximum height of the water film is independent of *AR* when it is sufficiently high that the water film cannot converge completely before the projectile fully submerges. To investigate this feature further, the liquid film height (h/D), i.e. the z-position in figure 7, is shown as a function of time in figure 8. For both $U_\circ$ values, the general trend of the variation of h/D with *AR* is similar. That is, the initial speed (at $t^* < 1.0$) of a rising film is almost identical ($\partial h^*/\partial t^* \simeq 0.7$ and 0.6 for $U_\circ = 2.5$ m s^{-1} and 4.2 m s^{-1}, respectively) for all *AR* values, but the slope during the falling stage is different. After the maximum height, the falling velocity decreases with increasing *AR*; $\partial h^*/\partial t^* = -0.51$, -0.44, -0.21 and -0.17 for $U_\circ = 2.5$ m s^{-1}, and -0.61, -0.52, -0.20 and -0.10 for $U_\circ = 4.2$ m s^{-1} when $AR = 1.0$, 2.0, 4.0 and 8.0, respectively. The maximum height of the water film remains constant at $h/D \simeq 0.8$. For *AR* 1–2, the film height decreases sharply after the water film closes at the rear pole of the projectile; thus, the maximum height is less than $0.8D$ (figure 8). As *AR* increases to 4.0, h/D increases to the maximum of 0.8 and then decreases gradually. At $t^* \simeq 3.5$, similar to the cases with lower *AR* values, the water film experiences a sharp fall after it gathers around the rear

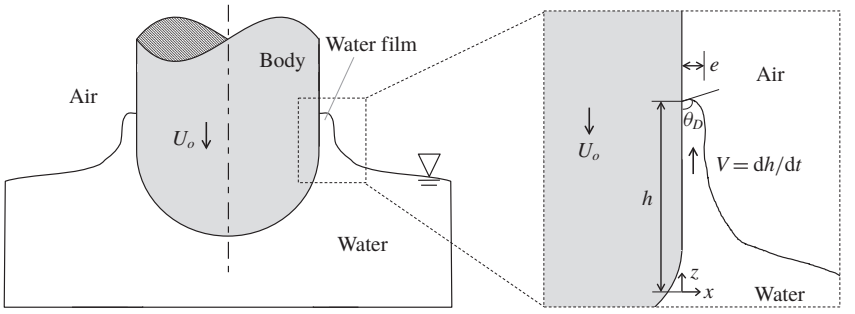

FIGURE 9. Schematic diagram of the ascending water film on the surface of an impacting body: h is measured from the undisturbed free surface. The thickness of the water film is defined as e.

pole. For AR 8, the water film falls down to the free surface at a constant rate after reaching the maximum height of $0.8D$. Interestingly, the critical non-dimensional time for classifying these different rising water film behaviours depending on the AR is similar even if the impact velocity increases to 4.2 m s^{-1} (figure 8b).

If a thin jet is not formed through water film convergence at the rear pole, the maximum height of a water film is fixed at $h/D \simeq 0.8$. To study this behaviour, we simplified the problem of a water film rise along the surface of an impacting body (figure 9). As shown, it is assumed that the water film rises along the body surface with a constant thickness (e), which is very thin compared to the body size ($D = 2R$), while the body moves downward at $U_\circ$. The distance to the end of water film from the undisturbed free surface is defined as h. In this situation, the inertia transferred from the impacting body drives the motion and the capillary (F_c), viscous (F_v) and gravitational (F_g) forces resist it (3.1):

$$\frac{\mathrm{d}}{\mathrm{d}t}\left(m_f \frac{\mathrm{d}h}{\mathrm{d}t}\right) = F_c - F_v - F_g. \tag{3.1}$$

Here, m_f is the mass of the water film, and the capillary and gravitational forces are given by $F_c = 2\pi R\sigma \cos\theta_D$ and $F_g = m_f g = 2\pi\rho Rehg$, respectively ($\sigma$: surface tension, θ_D: dynamic contact angle, g: gravitational acceleration). To calculate the viscous force, it is necessary to know the velocity distribution inside the water film. Since the water film is quite thin, it is assumed that the vertical (z) component of the velocity ($v = v(x)$) is dominant. We also consider that the film flow on a moving surface is fully developed, with boundary conditions of $v(0) = -U_\circ$ and $\mathrm{d}v/\mathrm{d}x(e) = 0$. Thus, the water film velocity at the interface to the ambient air is considered to be the same as the velocity at which the water film rises (similar to a Couette flow). The velocity distribution inside the water film and the corresponding viscous force at the body surface are given by (3.2) and (3.3), respectively:

$$v(x) = \left(\frac{\mathrm{d}h}{\mathrm{d}t} + U_\circ\right)\left(2 - \frac{x}{e}\right)\frac{x}{e} - U_\circ, \tag{3.2}$$

$$F_v = \int \tau_w = a_1 \frac{4\pi R\mu}{e} h \frac{\mathrm{d}h}{\mathrm{d}t} + a_2 \frac{4\pi R\mu U_\circ}{e} h. \tag{3.3}$$

Here, the pre-factors of a_1 and a_2 are introduced to compensate for the possible deviations from the assumptions of fully developed flow and constant water film

thickness. Das *et al.* (2014) used similar pre-factors to compensate for the deviations of the velocity profiles from the assumed one in the capillary rise of an electrolytic solution. These pre-factors play the role of fitting parameters in actual application, and they were determined by the least square error method. Collecting these relations, equation (3.1) can be written as (3.4):

$$\frac{\mathrm{d}^2h}{\mathrm{d}t^2} = \left(\frac{\sigma\cos\theta_D}{\rho e}\right)\frac{1}{h} - a_1\frac{2\mu}{\rho e^2}\left(\frac{\mathrm{d}h}{\mathrm{d}t}\right) - \left(a_2\frac{2\mu U_\circ}{\rho e^2} + g\right) - \frac{1}{h}\left(\frac{\mathrm{d}h}{\mathrm{d}t}\right)^2. \tag{3.4}$$

This equation can be further normalized for the dimensionless height ($h^* = h/D$) as

$$\frac{\mathrm{d}^2h^*}{\mathrm{d}t^{*2}} = \left(\frac{\sigma\cos\theta_D}{\rho e}\right)\frac{1}{U_\circ^2}\frac{1}{h^*} - a_1\frac{2\mu}{\rho e^2}\frac{D}{U_\circ}\left(\frac{\mathrm{d}h^*}{\mathrm{d}t^*}\right) - \left(a_2\frac{2\mu U_\circ}{\rho e^2} + g\right)\frac{D}{U_\circ^2} - \frac{1}{h^*}\left(\frac{\mathrm{d}h^*}{\mathrm{d}t^*}\right)^2. \tag{3.5}$$

For e and θ_D, we obtained the values from the measured data. First, we measured the film thickness over time, which was almost constant ($e/D \simeq 0.02$) during the rise and got thicker ($e/D \simeq 0.03$) as the film fell (see figure S1 in the supplementary material). Based on this, we assumed that e is constant and used a time-averaged thickness of 0.8 mm and 0.11 mm for $U_\circ = 2.5$ m s^{-1} and 4.2 m s^{-1}, respectively. On the other hand, θ_D would change over time as well, but we were not able to measure it accurately (measured values were scattered in the range of 110°–150°) due to the limited resolution near the contact line. Thus, we measured the static contact angle of a water droplet ($\theta_c = 74°$) on the side wall of the *AR* 8 projectile, and used a dynamic contact angle model given by $\theta_D^3 = \theta_c^3 + 144Ca$ (Cox 1986). As a result, θ_D was estimated as 110° and 125° for $U_\circ = 2.5$ m s^{-1} and 4.2 m s^{-1}, respectively. These values were used as a representative (constant) θ_D.

Designating $t^* = 0$ as the instant at which the rise of the water film can first be distinguished visually, the initial conditions of $h^*(0)$ and $\mathrm{d}h^*/\mathrm{d}t^*(0)$ were calculated from the measured data. These initial conditions were found to have positive values, indicating that the initial driving force of the film rise is the strong inertia transferred from the impacting body. After putting these empirical values into (3.5), it was numerically solved using the fourth-order Runge–Kutta method. The pre-factors were found to be $(a1, a2) = (15, 2.8)$ and $(77, 5.6)$ for $U_\circ = 2.5$ m s^{-1} and 4.2 m s^{-1}, respectively. The results of the estimated water film height for the case of *AR* 8 are plotted together in figure 8, in which the present estimates show reasonable agreement with the measured water film heights. This also indicates that our assumptions are reasonable. As the impact velocity increases, the deviation between the measurement and estimate slightly increases. Since we assumed a constant film thickness, the effect of a curved edge near the free surface would be non-negligible with increasing inertia of the projectile. The first, second, third and fourth terms on the right-hand side of (3.5), on the other hand, represent the contributions of surface tension, viscosity, gravity and added water film mass from the pool, respectively. After comparing the magnitudes of these components, it was found that the inertia drives the initial motion at $t^* < 1.0$, which is counteracted by a capillary force and large initial mass of rising water film. As time progresses, the inertia of the rising water film is reduced, and it is balanced by the surface tension, viscous force and gravity at $t^* \simeq 1.2$–1.5. After that, the viscous force (together with gravity) drives the downward fall of the water film (figure 8). Since the inertia dominates the flow for a very short time only during the initial stage, as shown above, the general trend of a moving water film does not vary significantly with $U_\circ$ (figures 7 and 8).

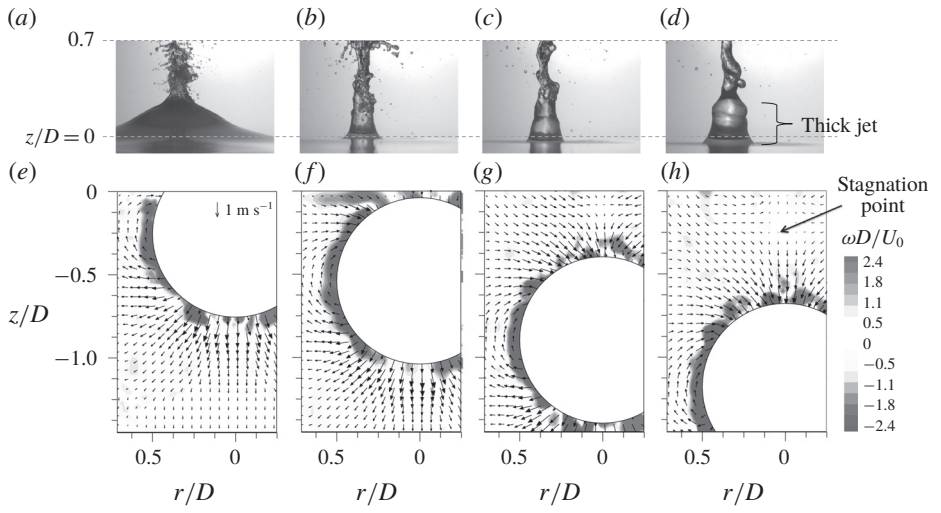

FIGURE 10. (Colour online) Generation of a thick jet (*a–d*) and the flow structures below the free surface (*e–h*) at: (*a*,*e*) $t^* = 0.8$; (*b*,*f*) 1.2; (*c*,*g*) 1.6; (*d*,*h*) 2.0. The considered case is $U_\circ = 2.5$ m s^{-1}, $AR = 1$ with a smooth surface.

3.3. *Thick jet formation*

As it is shown most clearly in figure 2(*b*), a thick jet is induced after thin jet formation. While its shape differs slightly depending on the *AR*, it can be said that the tip of a thick jet tends to collapse into a disk-like shape below the thin jet for $AR = 1.0$–4.0. When $AR = 8.0$, the jet flow originates from a different mechanism, i.e. the collapse of a quasi-static cavity. To understand the process of thick jet formation, we measured the liquid (water) phase velocity below the free surface at the instants at which thick jets were formed above the free surface, using particle image velocimetry. The measured velocity and vorticity fields are shown together with the corresponding jet flow in figures 10–12. As the sphere (*AR* 1) moves through the water surface, it pushes the surrounding water away (figure 10*e*), which turns around toward the rear side as it descends (figure 10*f*,*g*,*h*). Thus, the water flow induced by the sinking sphere resembles that of a doublet, as mentioned by Kubota & Mochizuki (2011). Due to the interaction between this flow structure and a free surface, a stagnation point appears below the free surface (indicated with an arrow in figure 10*h*), and substantial upward flow is induced above this point, resulting in a thick (secondary) jet. As shown in the figures, the generation of a thick jet is well synchronized with the appearance of a stagnation point below the free surface. Previously, Kuwabara *et al.* (1987) observed a similar phenomenon and mentioned that the secondary jet is related to high-speed water flow toward the sphere centre. As this thick jet falls down into the free surface, it forces the free surface to sag (figure 3*a*,*b*). For the cases of *AR* 2–4, the same thick jet formation mechanism is applied as the stagnation point shows up between the free surface and body tail (figures 11*h*, 12*h*). When $AR = 4.0$, the flow displaced by the front side of the body is not directly connected to the flow toward the rear side (figure 12*e*) but the low pressure region in the wake behind the sinking body induces a stagnation point in the flow, resulting in a thick jet (figure 12*b*,*f*,*c*,*g*,*d*,*h*). Since the motion of a displaced fluid around the front part of the body contributes strongly to the generation of upward flow, it becomes weaker

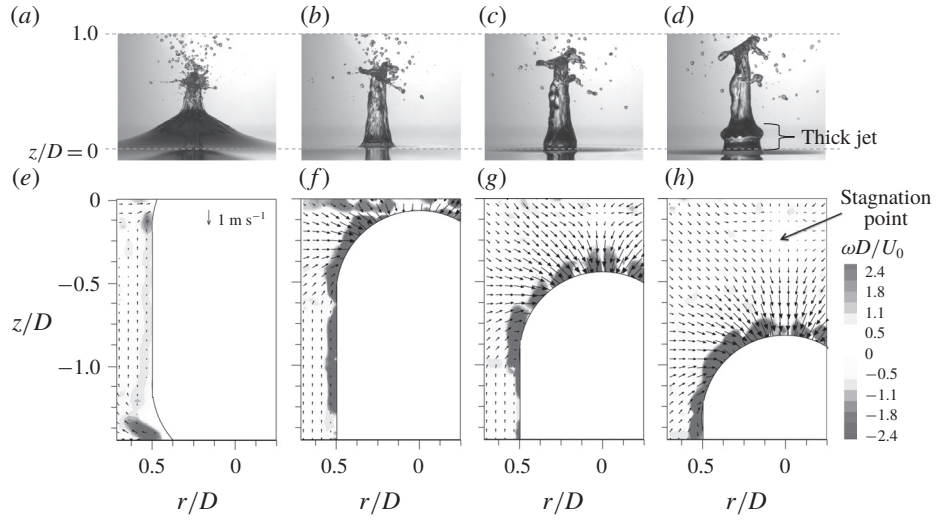

FIGURE 11. (Colour online) Generation of a thick jet (*a–d*) and the flow structures below the free surface (*e–h*) at: (*a*,*e*) $t^* = 1.8$; (*b*,*f*) 2.2; (*c*,*h*) 2.6; (*d*,*h*) 3.0. The considered case is $U_\circ = 2.5$ m s^{-1}, $AR = 2$ with a smooth surface.

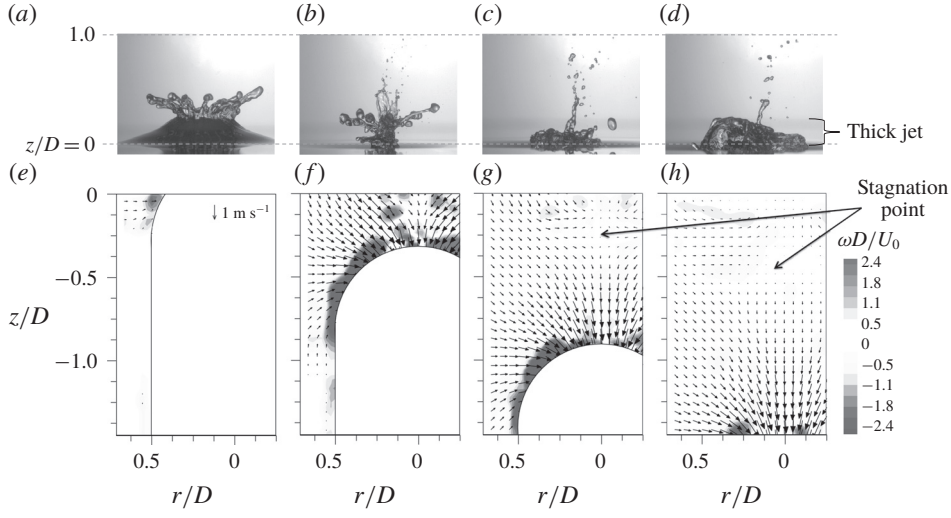

FIGURE 12. (Colour online) Generation of a thick jet (*a–d*) and the flow structures below the free surface (*e–h*) at: (*a*,*e*) $t^* = 3.6$; (*b*,*f*) 4.2; (*c*,*g*) 4.8; (*d*,*h*) 5.4. The considered case is $U_\circ = 2.5$ m s^{-1}, $AR = 4$ with a smooth surface.

as AR increases. Thus, the height of a thick jet decreases with increasing (decreasing) AR ($U_\circ$).

3.4. *Jet-tip breakdown*

So far, we have discussed the processes of thin and thick jet formation. Interestingly, the jet tip breaks down in some cases (figures 2*a*,*b*, and 3*a*). When $U_\circ = 2.5$ m s^{-1},

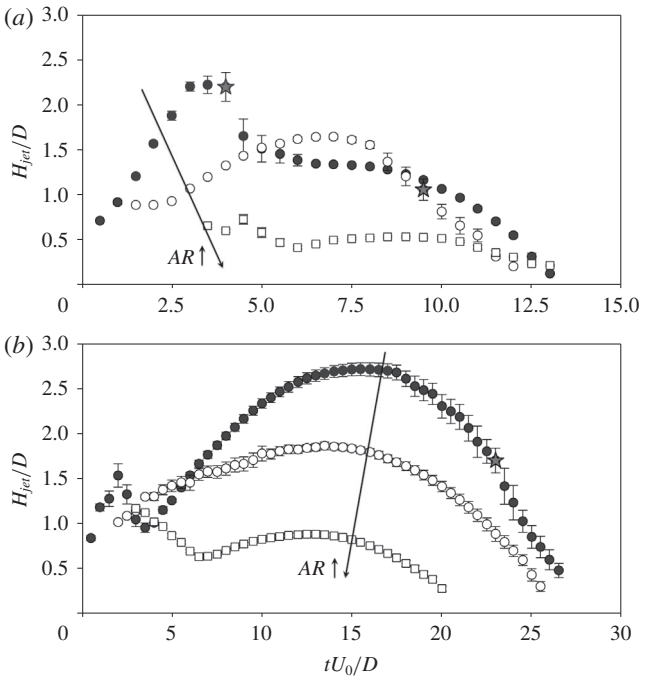

FIGURE 13. (Colour online) Temporal variation of the continuous jet height (H_{jet}) measured from the free surface: (*a*) $U_\circ = 2.5$ m s^{-1}; (*b*) 4.2 m s^{-1}. ●, *AR* 1; ○, *AR* 2; □, *AR* 4. The star symbols denote the breakdown of the corresponding jet.

breakdown occurs for *AR* 1 and *AR* 2, and it is clearly visible for *AR* 1 at $U_\circ =$ 4.2 m s^{-1}. In figure 13, the temporal variation of a continuous (without a breakdown) jet height (H_{jet}) is plotted. Since the jet flow for the case of *AR* 8 has a different origin than that discussed here, it is not included in this figure. Roughly speaking, H_{jet} decreases with increasing *AR*, because the momentum of the impacting body is transferred to the jet faster as *AR* decreases. For *AR* 1, thin jet breakdown occurs at $t^* \simeq 4.0$ and 23.0 for $U_\circ = 2.5$ m s^{-1} and 4.2 m s^{-1}, respectively (sharp decreases of H_{jet} are denoted with star symbols in the figure). For $U_\circ = 2.5$ m s^{-1}, H_{jet} was measured for thin and thick jets before and after breakdown, respectively. When $U_\circ =$ 4.2 m s^{-1}, the initial steep slope indicates the rise of a thin jet and the second gentle increases corresponds to the rise of a thick jet (figure 13*b*). In the case of *AR* 2, distinguishable jet breakdown occurs only when $U_\circ = 2.5$ m s^{-1} (at $t^* \simeq 9.5$); at $U_\circ =$ 4.2 m s^{-1}, the thin jet breaks into small droplets as soon as it is formed.

The necking of liquid jets is well known in relation to the role of surface tension, such that the perturbation on a liquid filament surface grows at a critical condition (Rayleigh–Plateau instability) (Plateau 1873; Rayleigh 1878). To assess the breakdown of the present jet flows, the relevant parameters are summarized in table 2. The equivalent radius (R_t) of the jet tip was measured at the moment that the jet reached the maximum height ($H_{jet,max}$). We measured R_t by assuming that the jet-tip shape is spherical. The corresponding value of the Ohnesorge number ($Oh = \mu/(\rho R_t \sigma)^{0.5}$) was obtained in each case, which indicates the ratio of the viscous time scale to the capillary time scale and has been employed as an important variable in the pinch-off of viscous liquid filaments (Notz & Basaran 2004; Eggers & Villermaux

$U_\circ$ (m s^{-1})	AR	R_t (mm)	Oh	$L_\circ$
2.5	1.0	2.3 ± 0.31	0.0024	21.9
	2.0	3.8 ± 0.49	0.0019	8.8
	4.0	11.3 ± 1.3	0.0011	1.0
4.2	1.0	5.4 ± 0.41	0.0016	10.0
	2.0	7.6 ± 0.82	0.0013	4.8
	4.0	11.7 ± 2.43	0.0011	1.5

TABLE 2. Measurement of R_t at $H_{jet,max}$. The corresponding values of Oh and $L_\circ = H_{jet,max}/(2R_t)$ were calculated.

2008; Driessen *et al.* 2013). As AR increases, Oh tends to decrease for both impact velocities (table 2).

Finally, the aspect ratio of a jet is defined as $L_\circ = H_{jet,max}/(2R_t)$. Notz & Basaran (2004) investigated the critical condition of liquid filament breakup and found that the critical $L_\circ$ for jet breakdown increases with increasing Oh, below which the liquid film does not break. They reported that the critical $L_\circ$ is 5.5 ± 0.5 for $Oh \simeq 0.001$. In the present results, jet pinch-off occurred in the cases of AR 1–2 when $U_\circ = 2.5$ m s^{-1} and AR 1 when $U_\circ = 4.2$ m s^{-1}, in which cases $L_\circ$ is larger than about 5.0 and Oh is slightly larger than 0.001 (table 2). As shown in figure 4, the present breakdown occurs mostly in the form of end pinching (jet-tip breakdown) (Stone, Bentley & Leal 1986), which has been suggested as a main cause at $Oh \lesssim 0.1$ (Driessen *et al.* 2013). Thus, it is understood that the viscosity influenced the jet breakdown in the present cases. At $Oh \gtrsim 0.1$, breakdown will occur due to the Rayleigh–Plateau instability. The existence of a critical aspect ratio also indicates that there is a relation between the inertia and capillary forces. That is, R_t is associated with the capillary force and $H_{jet,max}$ is related to the lifetime (inertia) of a jet. As AR increases, R_t increases and the jet rise velocity decreases. As R_t decreases, the jet becomes more susceptible to breakdown. Jet pinch-off was not observed for $AR \geqslant 4.0$ and $AR \geqslant 2.0$ when $U_\circ =$ 2.5 m s^{-1} and 4.2 m s^{-1}, respectively, which supports this interpretation.

4. Water entry of a projectile with a cavity

4.1. *Overall description of the free-surface deformation*

In this section, we describe the water entry of a projectile with a rough front. Except the roughness (figure 1*b*), the other conditions were same as those considered in § 3. The representative temporal evolutions of a splash (jet) and cavity are shown for $U_\circ = 2.5$ m s^{-1} (figure 14) and 4.2 m s^{-1} (figure 15). Compared to the case with a smooth front part (figures 2 and 3), the differences in the free-surface deformation are clear in terms of an underwater cavity and a splash above the free surface. For the cases considered, a splash is generally formed after impact ($t^* < 1.0$ and $t^* < 2.0$ for $U_\circ = 2.5$ m s^{-1} and 4.2 m s^{-1}, respectively) (figures 14 and 15), which developed from horizontal ejecta, as explained by Truscott *et al.* (2014). As time progresses, the splash evolves further and converges into a dome, followed by the necking (or pinch-off) of an underwater cavity. For the case of AR 8, the projectile itself interferes with the processes of dome closure and cavity pinch-off (figures 14*d*, 15*d*). The cavity pinch-off induces two vertical jets: one is forced upward through the dome and the other is ejected downward toward the falling projectile. Later, the splash and

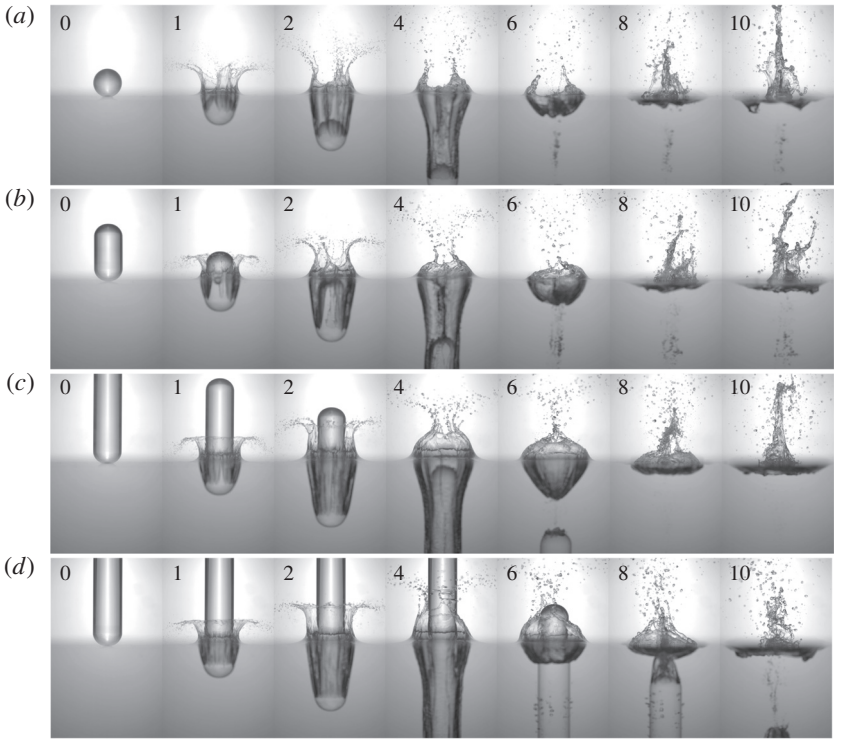

FIGURE 14. Splash and cavity formation by the water entry of a body with a rough surface at $U_\circ = 2.5$ m s^{-1}: (*a*) $AR = 1.0$; (*b*) 2.0; (*c*) 4.0 and (*d*) 8.0. The numbers in each image denote t^*.

upward jet break down in a complex manner. Compared to the case of $U_\circ = 4.2$ m s^{-1} (figure 15), the shapes of the splash and cavity, for $U_\circ = 2.5$ m s^{-1}, are less organized (i.e. axisymmetry is disturbed and the dome closure is not completed); thus, their volumes are reduced at a lower $U_\circ$ (figure 14).

In figure 16, the process of splash formation for the case of *AR* 1 is shown for both impact velocities. With a smooth surface, the water film rises along the body surface and converges at the rear pole (figure 6); however, it cannot move along the rough surface and instead separates early to create a splash shortly after the projectile impacts the free surface. It should be noted that the separation of a water film also occurs from a smooth body surface if the inertia of the impacting body is sufficiently large (Thoroddsen *et al.* 2004). Latka *et al.* (2012) performed an experiment in which a liquid droplet impacted a rough surface, producing a splash immediately after the collision. As the roughness increases, droplets are strongly prevented from transforming into thin liquid sheets and early splashing at the advancing contact line is encouraged. This phenomenon has been attributed to a large force required for the liquid to penetrate into the voids between roughness features while climbing the body surface (Kubiak *et al.* 2011). Similarly, in the present case, the roughness of the sphere surface prevents water from forming a stable liquid film on it but encourages an early separation to create a splash. On the other hand, the speed of a water film is lower at a lower impact velocity, enabling it to move further along the body surface without being affected by the surface roughness (figure 16*a*). Zhao *et al.*

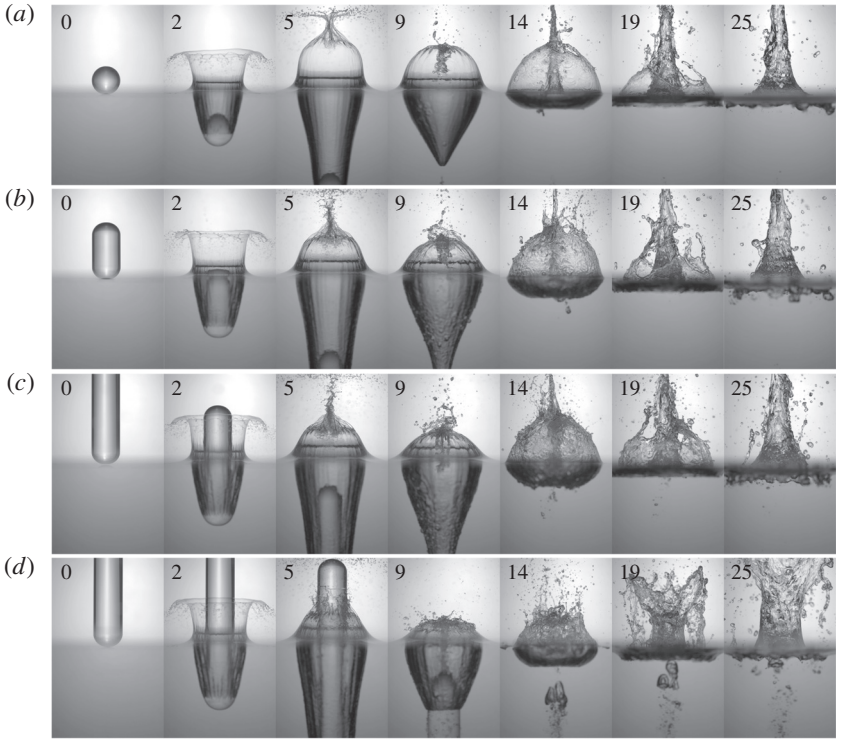

FIGURE 15. Splash and cavity formation by the water entry of a body with a rough surface at $U_\circ = 4.2$ m s^{-1}: (*a*) $AR = 1.0$; (*b*) 2.0; (*c*) 4.0 and (*d*) 8.0. The numbers in each image denote t^*.

(2014) reported that a splash is not formed in the water entry of a sphere even when the surface is rough if the impact velocity is sufficiently low that the water film can fully fill the voids between roughness features. Since we applied randomly distributed roughness features, the separation position of a water film differs locally around the periphery (figure 16*a*). This non-uniformity of the roughness causes asymmetry of the splash (and underwater cavity), which decreases with increasing $U_\circ$ (figure 16*b*).

4.2. *Splash and underwater cavity formation*

To quantity the effects of AR and $U_\circ$ on splash and cavity formation, the temporal variations of the height (H_s) and width (W_s) of a splash are plotted in figures 17 and 18, respectively. Here, we used the portion of a continuously connected water film in a splash, detected by applying a binarization and a Wiener filter to the raw images. H_s is defined as the vertical distance from the free surface to the highest position in the detected water film and the horizontal distance between them was designated as W_s (see the insets in figures 17 and 18). After dome closure, the positions at which the Worthington jet crosses the dome are used to determine H_s, and W_s is measured until the dome is closed. The splash size tends to increase with increasing AR for lower $U_\circ = 2.5$ m s^{-1} (figures 17*a*, 18*a*), but the tendency is reversed for $U_\circ = 4.2$ m s^{-1} (figures 17*b*, 18*b*). As mentioned above, the water film separates later by filling some of the voids between roughness features when $U_\circ$ is low. Since the sinking velocity

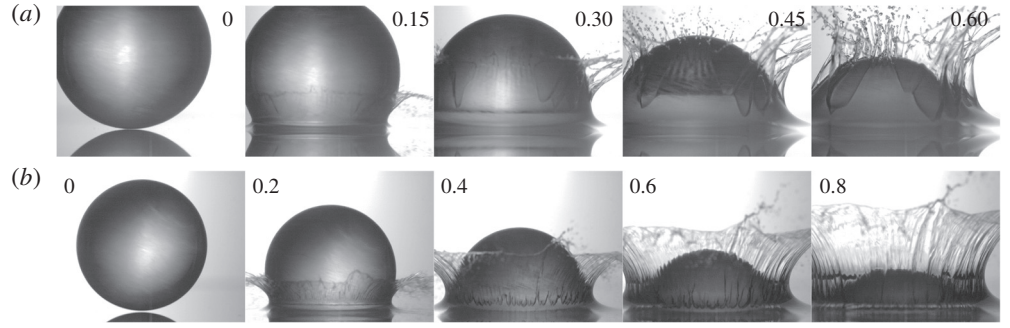

FIGURE 16. Splash formation above a free surface upon the water entry of a body (with a rough surface) at (*a*) $U_o = 2.5$ m s^{-1} and (*b*) 4.2 m s^{-1}. The numbers in each image denotes t^*.

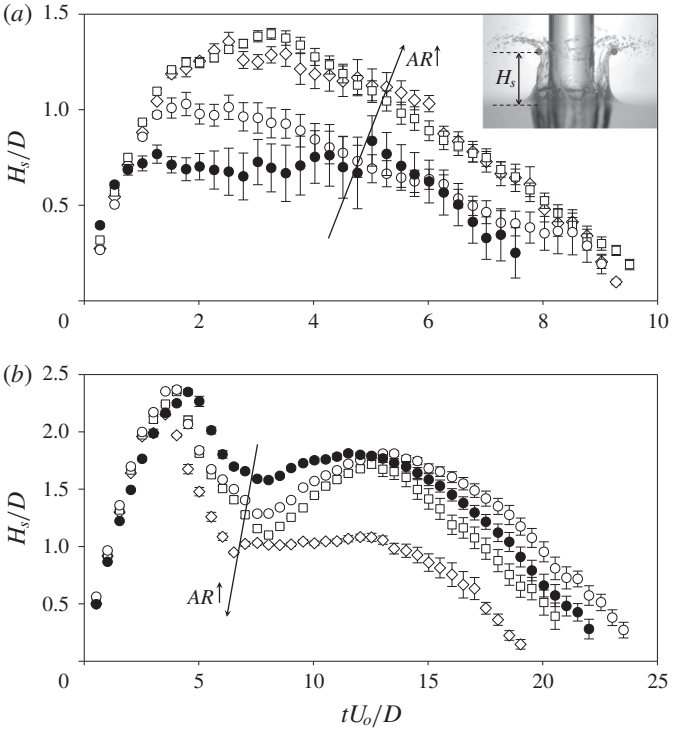

FIGURE 17. (Colour online) Temporal variation of H_s: (*a*) $U_\circ = 2.5$ m s^{-1}; (*b*) 4.2 m s^{-1}. ●, *AR* 1; ○, *AR* 2; □, *AR* 4; ◇, *AR* 8.

of a projectile increases with increasing *AR* (see figure 23), there is not enough time for the liquid film to fill the voids on a rough surface. The downward velocity of a nose immediately after impact ($t^* < 5.0$) exhibits the same trend as that shown in figure 23. Consequently, the separation occurs earlier and the splash volume increases. Thus, the case of *AR* 1 has the shortest splash height and width when $U_\circ = 2.5$ m s^{-1}. At this $U_\circ$, the splash height increases to a peak and then decreases (figure 17*a*). The maximum height increases with increasing *AR* and becomes almost the same

for AR 4 and AR 8. W_s follows a trend similar to that of H_s and remains constant at later times (figure 18*a*). The maximum width also increases with increasing AR. When $U_\circ = 4.2$ m s^{-1}, on the other hand, the water film separates earlier and thus the splash size increases sharply at $t^* < 3.0$. The variation among AR values is negligible, indicating that the separation position of the water film is not affected, and the splash grows to almost the same maximum height and width (figures 17*b*, 18*b*). After the splash converges into a dome, its height decreases ($5.0 \lesssim t^* \lesssim 7.0$). Subsequently, the upward Worthington jet is ejected to the free surface due to the pinch-off of an underwater cavity, by which the air contained in the cavity pops up, resulting in a slight increase of H_s at $t^* = 7.0$–15.0. In figure 15 (at $t^* = 9.0$ and 14.0), the air inside the upper cavity after the pinch-off moves together with the vertical jet and the dome expands. The Worthington jet also exists at $U_\circ = 2.5$ m s^{-1}, but no secondary peak of H_s exists (figure 17*a*) due to the incomplete dome closure (figure 14). Finally, H_s decreases as the dome collapses at $t^* > 15.0$. In the case of AR 8, the secondary peak is not clearly observable and its magnitude is smaller than it is in the other cases. As shown in figure 15(*d*), the long projectile shape disturbs the completion of dome closure (and cavity pinch-off). However, the increase in jet height at $t^* = 19.0$ (figure 15*d*) is attributed to the annular jet caused by the entry of a long cylindrical body. On the other hand, the slopes of decreasing H_s are almost the same for all AR values (figure 17*b*). As the splash forms, W_s increases to the maximum (again the ascending slopes are not affected by AR) and then decreases to form a dome (figure 18*b*). As AR increases, it takes less time to form a dome (i.e. $W_s/D = 0$). Since the splash impacts the side wall of the projectile while it transforms into a dome, the splash width saturates to $W_s/D = 1.0$ for the case of AR 8.

Under the free surface, cavity pinch-off occurs, as shown in figure 19 (see supplementary movie S2 as well). A typical deep seal is observable for AR 1–2, but an additional pinch-off occurs first at the side wall of the projectile for $AR \geqslant 4.0$. As $U_\circ$ increases, the cavity formation and subsequent pinch-off process occur symmetrically. Figure 20 depicts the cavity volume (V_c) calculated by assuming its axisymmetry; that is, the outer profiles of the cavity and projectile were revolved and their volumes were subtracted to obtain these values (see the inset in figure 20). The projectiles of AR 4–8 at $U_\circ = 2.5$ m s^{-1} have very small (and almost constant) cavity sizes initially, but the size suddenly increases (figure 20*a*). In these cases, the low impact velocity provides a momentum that is insufficient to create a well-defined cavity; thus, the initial cavity is small. As the cavity shrinks after the pinch-off, a portion of air bubble sticks to the tail, which is dragged by the falling body (at $t^* = 4.0$–4.6 in figure 19*c*). Consequently, the cavity size appears to increase suddenly. On the other hand, the projectiles of AR 1–2 have much larger cavities, which increase in size from the beginning. In these cases, the body occupies smaller portions of the cavity than in the cases of AR 4–8. For AR 1–2, the cavity expands to the peak, after which the air pressure becomes lower than the hydrostatic pressure of the surrounding water, and then shrinks gradually and necking occurs (figure 20*a*). When $AR = 1.0$, the cavity is larger and necking occurs earlier than AR 2.

When $U_\circ = 4.2$ m s^{-1} (figure 20*b*), the initial ($t^* \lesssim 3.5$) cavity size is almost the same. At $t^* > 4.0$, the V_c increases as AR increases (except AR 8), because the additional air is pushed down to the cavity while the dome is formed above a free surface. As shown in figure 17(*b*), H_s decreases at $t^* = 4.0$–7.0, while the splash crown collapses into a dome. As the splash converges, air is pushed around inside the cavity. H_s decreases with increasing AR, inducing cavity expansion. For the largest AR of 8.0, both dome closure and cavity pinch-off occur on the side wall

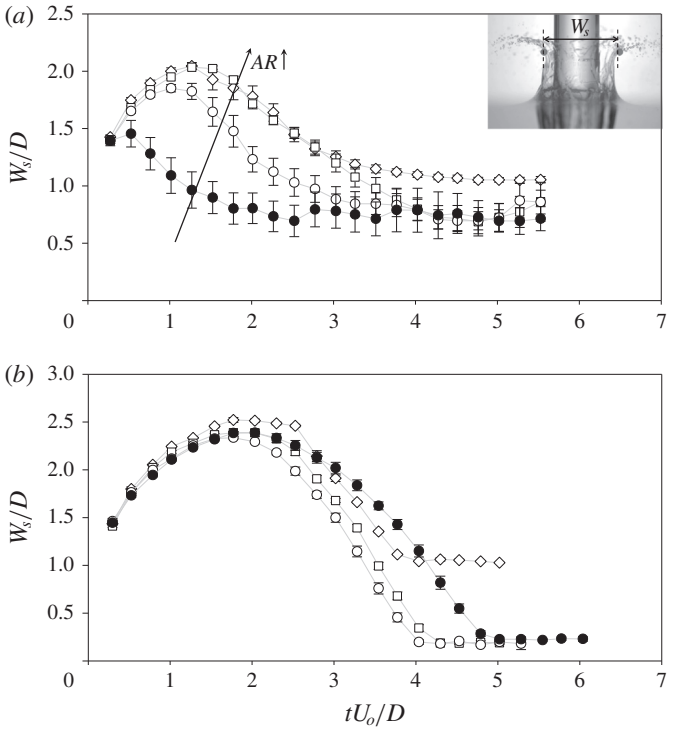

FIGURE 18. (Colour online) Temporal variation of W_s corresponding to H_s: (*a*) $U_\circ = 2.5$ m s^{-1}; (*b*) 4.2 m s^{-1}. ●, *AR* 1; ○, *AR* 2; □, *AR* 4; ◇, *AR* 8.

of the body, indicating that they occur earlier than they do with the other *AR* values. Consequently, the cavity with *AR* 8 is less developed and small. The cavity is the smallest when $AR = 1.0$, because dome closure occurs the latest among the test cases, and the cavity contraction due to hydrostatic pressure is stronger than the expansion due to the dragged air.

Meanwhile, the instant at which the cavity size reaches the maximum occurs earlier as *AR* decreases, except for *AR* 8, agreeing with the observation that cavity contraction and pinch-off occur earlier as *AR* decreases. After the cavity pinch-off, the Worthington jet pops up and the splash height increases ($t^* = 7.0$–13.0 in figure 17*b*). In particular, the domes are considerably larger for *AR* 2–4, because the cavity below the free surface is larger (figure 20*b*). This finding agrees with the fact that H_s increases to almost the same position at $t^* = 12.5$ in figure 17(*b*) when $AR = 1.0$–4.0. To support this observation, we calculated the sum of the cavity and dome volumes, V_c/D^3 and V_d/D^3, respectively, at $t^* = 5.0$, which has similar values of 11.0–12.5 for *AR* 1–4.

Since the measurement repeatability was better for $U_\circ = 4.2$ m s^{-1}, it was analysed further. We measured the instants of the dome closure (t_d) and cavity pinch-off (t_p). The positions of cavity pinch-off (H_p) and the centre of the hemispherical head (H), both measured from the free surface, and their ratio (H_p/H) were also calculated (table 3). For *AR* 1–4, dome closure occurs earlier but cavity pinch-off is delayed as *AR* increases. Since the underwater speed of a sinking projectile increases with increasing *AR* (see figure 23), H increases, resulting in a decrease of H_p/H. This

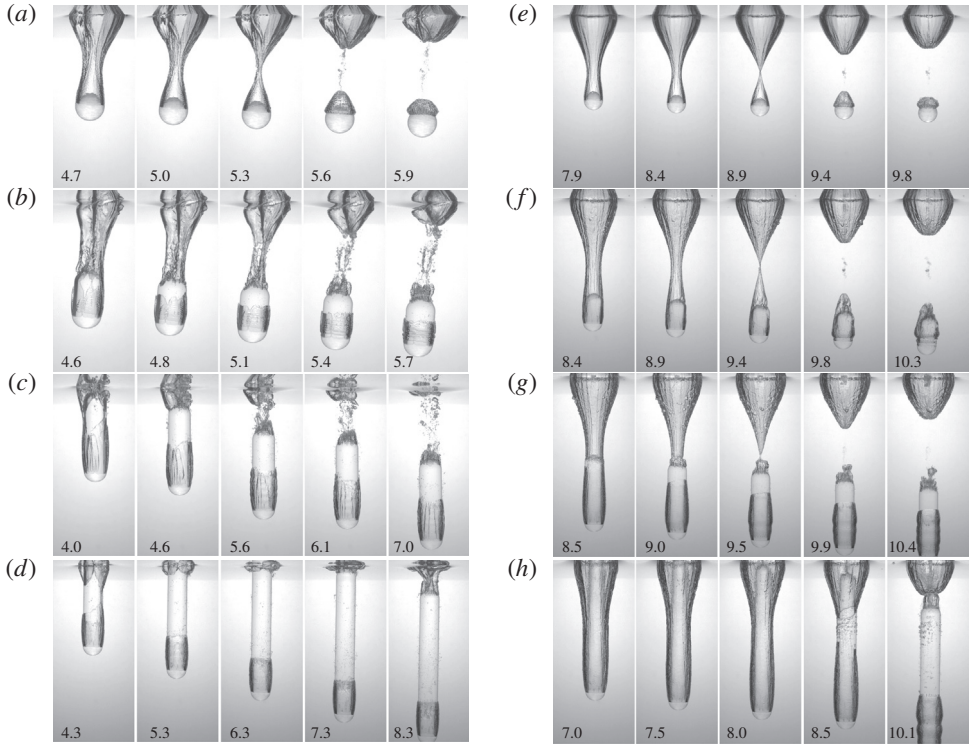

FIGURE 19. Process of a cavity pinch-off behind a body with a rough front surface at (*a–d*) $U_\circ = 2.5$ m s^{-1} and (*e–h*) 4.2 m s^{-1}: (*a*,*e*) *AR* 1, (*b*,*f*) *AR* 2, (*c*,*g*) *AR* 4, (*d*,*h*) *AR* 8. The numbers in each image denote t^*.

AR	$t_d U_\circ/D$	$t_p U_\circ/D$	H_p/D	H/D	H_p/H
1.0	4.91 ± 0.16	8.86 ± 0.01	2.79 ± 0.03	4.58 ± 0.03	0.61 ± 0.01
2.0	4.02 ± 0.10	9.35 ± 0.01	3.35 ± 0.03	6.78 ± 0.02	0.50 ± 0.01
4.0	4.17 ± 0.11	9.50 ± 0.04	3.87 ± 0.26	8.18 ± 0.03	0.47 ± 0.03
8.0	3.71 ± 0.04	8.04 ± 0.11	3.40 ± 0.09	7.57 ± 0.11	0.45 ± 0.01

TABLE 3. Measured values of t_d, t_p, H_p, H and H_p/H when $U_\circ = 4.2$ m s^{-1}.

behaviour is the same as that resulting from increasing the density of a sphere, as reported by Aristoff *et al.* (2010). They showed that cavity pinch-off occurs faster and closer to the free surface as the sphere density decreases. Thus, it is understood that the effective density of a projectile increases with increasing *AR*. For *AR* 1–4, only the nose of the projectile touches the cavity, but the effective mass increases with increasing *AR*. For *AR* 8, t_d and t_p are strongly disturbed by the projectiles and are therefore the shortest. Since the dome and cavity dynamics are affected by the surrounding pressure, we measured the air velocity induced by the entry of a sphere (*AR* 1) above the free surface (figure 21). It can be seen that a substantial amount of the surrounding air is dragged into the splash, due to the cavity expansion. Likewise, the velocity of the entrained air (v_a) was measured (immediately above the splash) for other *AR* values when the body tail passed the end of a splash. When averaged

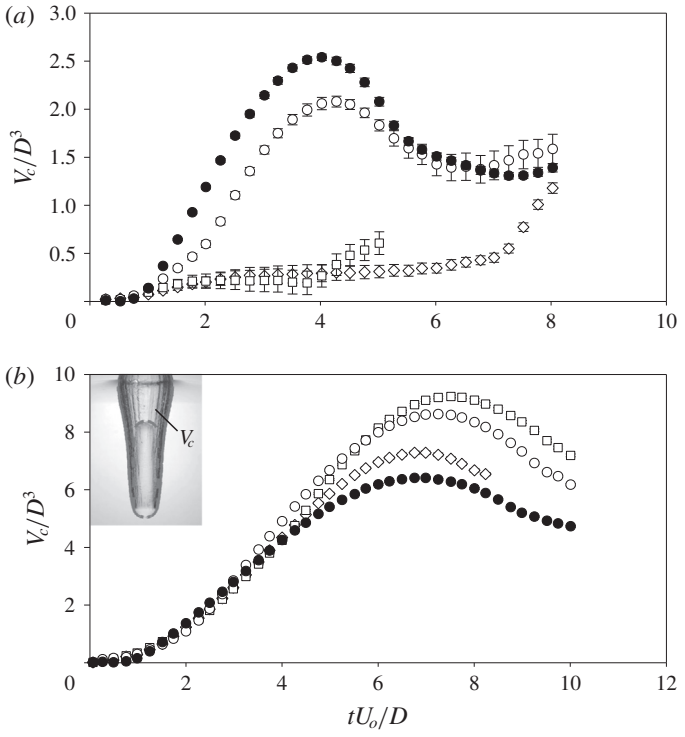

FIGURE 20. (Colour online) Temporal variation of V_c: (*a*) $U_\circ = 2.5$ m s^{-1}; (*b*) 4.2 m s^{-1}. ●, *AR* 1; ○, *AR* 2; □, *AR* 4; ◇, *AR* 8.

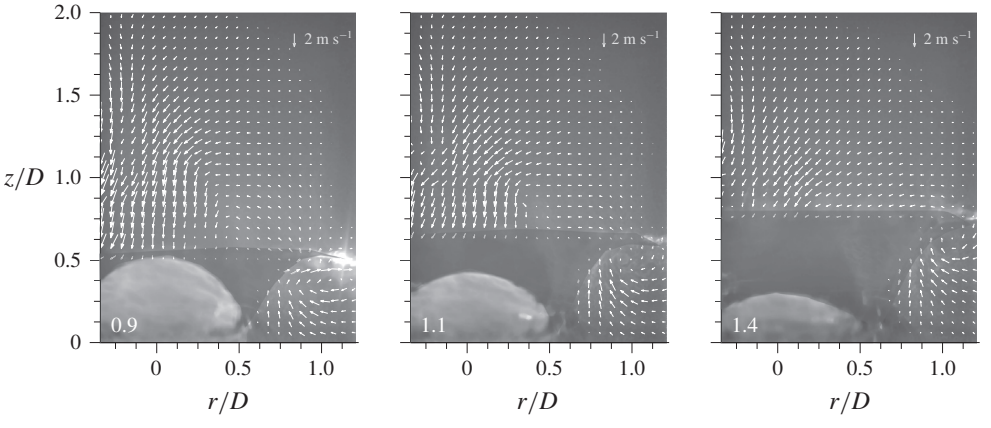

FIGURE 21. (Colour online) Airflow above a free surface during splash formation by a sphere when $U_\circ = 2.5$ m s^{-1}. The splash has been masked, and the numbers in each image denote t^*.

for $-0.35 \leqslant r/D \leqslant 0.35$, $v_a/U_\circ$ was found to be 0.14, 0.20 and 0.27 for *AR* 1, *AR* 2 and *AR* 4, respectively. According to the Bernoulli equation, the increased v_a induces

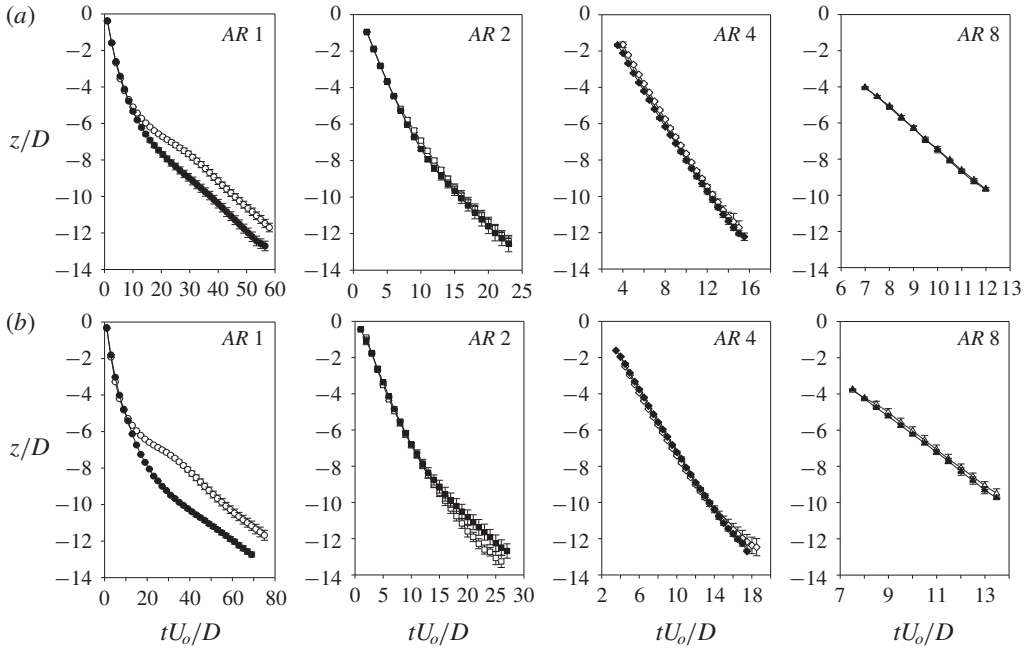

FIGURE 22. Temporal variation of the vertical (z) position of the centre of mass of the body: (a) $U_\circ = 2.5$ m s^{-1}; (b) 4.2 m s^{-1}. The open and closed symbols correspond to smooth and rough surfaces, respectively. $z = 0$ denotes the position of the undisturbed free surface.

a lower pressure, i.e. a greater pressure difference across the splash crown; thus, the dome closure is accelerated, as discussed by Marston *et al.* (2016).

5. Effects of a cavity on the dynamics of a sinking projectile

In this section, we further assess the effects of cavity dynamics, which strongly affect the trajectory (i.e. hydrodynamic force) of the body (Truscott *et al.* 2012; Shepard *et al.* 2014; Mansoor *et al.* 2017; Vakarelski *et al.* 2017). Figure 22 shows the vertical (z) position of the centre of mass of each projectile, which was measured as a midpoint between the centres of the spherical front and rear parts. To find these points, we binarized the raw images and applied a Wiener filter to highlight the outer profile. Then, we used a circle Hough transform to find the positions at which the probability of locating a circle was the highest. While matching to the size of the present projectile, the positions with the first and second highest probabilities were matched with the front and rear parts of the projectile. The velocity and acceleration of the projectile in the vertical direction are shown in figures 23 and 24, respectively. To calculate the velocity (or acceleration), it was first splined with a quintic function and differentiated (Truscott *et al.* 2012). For the case of *AR* 1, the initial sinking speeds of spheres with smooth and rough surfaces are almost the same, but they deviate at $t^* \simeq 10$ (for both $U_\circ$ values) which is the instant at which cavity pinch-off occurs. It is obvious that the body loses its momentum and decelerates due to buoyancy, as it sinks. However, after pinch-off, a downward jet is induced behind the body, which adds momentum; thus, the level of deceleration is less than it is

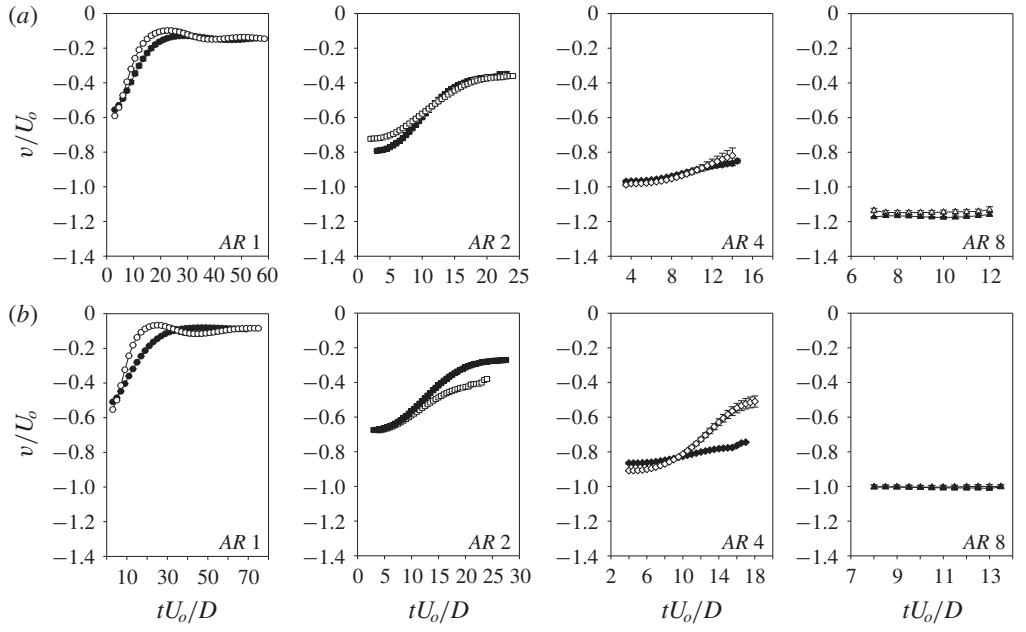

FIGURE 23. Temporal variation of the vertical velocity (v) of the body mass centre: (a) $U_\circ = 2.5$ m s^{-1}; (b) 4.2 m s^{-1}. The open and closed symbols correspond to smooth and rough surfaces, respectively.

for the smooth counterpart. Afterwards, the sinking slope becomes shallower and the sphere with a cavity travels farther in the vertical direction, while that with a smooth surface lags behind (figure 22). This trend can also be identified from the fact that the sinking velocity of a rough sphere is faster than that of a smooth sphere before it reaches terminal velocity (figure 23) (here the negative values denote downward velocities). Once terminal velocity is achieved, the difference between the two cases becomes small. Interestingly, when there is no cavity, the sinking velocity slightly increases and decreases again before reaching terminal velocity. Truscott *et al.* (2012) attributed this phenomenon to the momentum transfer from the vortex shedding in the wake (i.e. sort of wake-induced path instability of a falling body Ern *et al.* 2012), which is delayed in the cavity-forming case. As shown in figure 25(a), the smooth sphere experiences a transverse movement (while rotating) due to the asymmetry in the wake vortices (since this instability is beyond the scope of this study, we will discuss this effect only briefly). Due to this change, the smooth sphere experiences an acceleration-deceleration stage and then reaches a balanced state (i.e. zero acceleration) (figure 24). However, the sphere with a rough surface reaches terminal velocity without experiencing the additional deceleration stage, because the vortex shedding is suppressed by the cavity. In fact, similar path instability occurs later with a rough surface, indicating that it is delayed due to the underwater cavity.

Unlike the case of *AR* 1, there are no differences between the vertical position time histories corresponding to the smooth and rough surfaces for *AR* 2–4 (figure 22). However, the sinking velocity shows a deviation (figure 23). In the present measurement domain, the sinking velocity decreases earlier and converges, but the achievement of terminal velocity is not captured for $AR \geqslant 2.0$. For *AR* 2, the projectile with a rough surface sinks faster initially but behaves the same as that

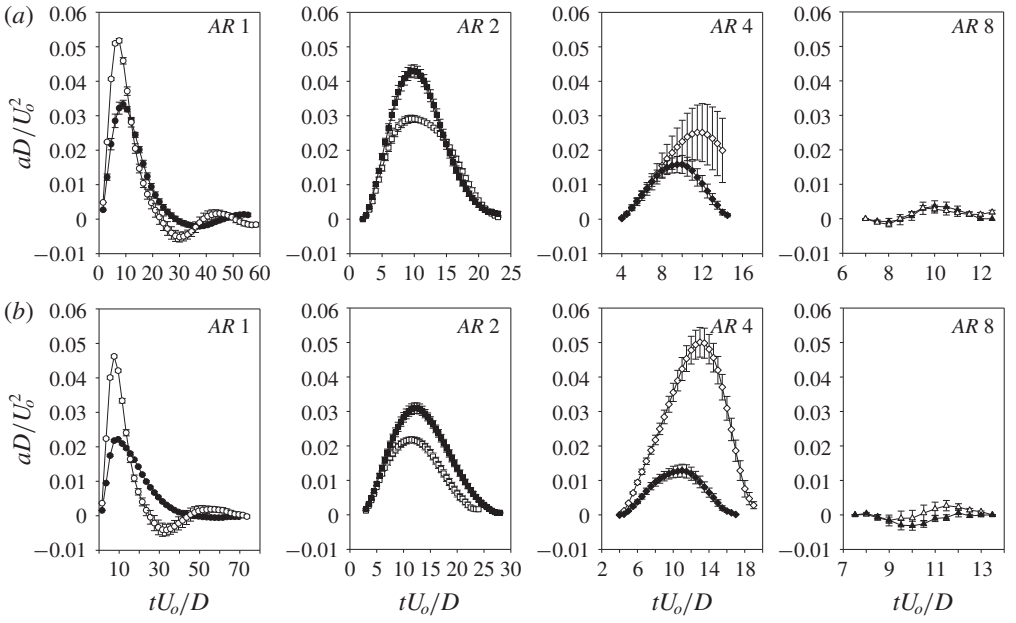

FIGURE 24. Temporal variation of the vertical acceleration (a) of the body mass centre: (a) $U_\circ = 2.5$ m s^{-1}; (b) 4.2 m s^{-1}. The open and closed symbols correspond to smooth and rough surfaces, respectively. Positive values denote acceleration in the upward direction (i.e. deceleration).

with a smooth surface later at a lower $U_\circ$. In the early stage, the underwater cavity works to reduce the drag acting on the body, so the rough surface projectile moves faster at $t^* < 14$ when $U_\circ = 2.5$ m s^{-1}. As the cavity departs away from the body after pinch-off, the sinking speed of the body with a rough surface becomes similar to that of the body with a smooth surface. Similarly to *AR* 1, the asymmetry in the wake causes the projectile to tumble, as shown in figure 25(b). In the measurement domain, the projectile with a smooth surface rotates twice during sinking, while that with a rough surface case does so only once (it is delayed due to the cavity). When $U_\circ = 4.2$ m s^{-1}, however, the projectile with a rough surface, which initially moves similarly to its smooth counterpart, decelerates more as time progresses (figure 23). In this situation, the projectile with a rough surface rotates once in our field of view as it sinks, while that with a smooth surface rotates three times (see supplementary movie S3). Although it is not clear why this trend is reversed even with the underwater cavity, we think that the relatively large amount of air attached to the body after the cavity pinch-off applies additional form drag to the body. However, this point should be investigated further in a future study. Despite the difference in the sinking-speed trends, for both $U_\circ$ values, the body with a rough surface decelerates more (figure 24), because of the large pressure drop in the wake after cavity pinch-off.

When $AR = 4.0$, the body with a smooth surface sinks slightly faster than that with a rough surface at first ($t^* \lesssim 12.0$) for both $U_\circ$ values, while this tendency is reversed later (figure 23). Similarly to *AR* 2, this behaviour occurs because the body with a smooth surface rotates (decelerates the body) earlier than that with a rough surface. For the largest *AR* of 8.0, the projectiles sink at constant velocities (within the present measurement region), and that with a rough surface moves slightly faster than that

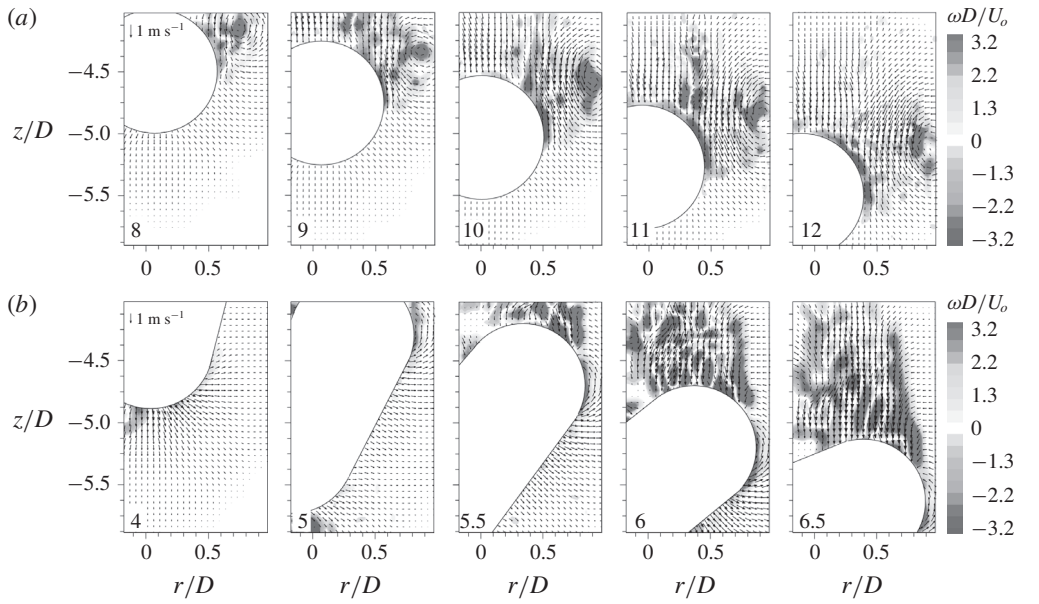

FIGURE 25. (Colour online) Underwater velocity fields and vorticity contours around a projectile with a smooth surface at $U_\circ = 2.5$ m s^{-1}: (*a*) *AR* 1, (*b*) *AR* 2. $z = 0$ denotes the position of the undisturbed free surface, and the numbers in each image denote t^*.

with a smooth surface (figure 23). The acceleration is quite small (almost zero) in both cases (figure 24).

Based on the vertical acceleration, the force coefficient (C_F) can be estimated using (5.1) (Mansoor *et al.* 2017):

$$C_F = \frac{F(t)}{\frac{1}{2}\rho A v(t)^2} = \frac{ma(t)}{\frac{1}{8}\rho \pi D^2 v(t)^2}. \tag{5.1}$$

Here, m is the mass of the projectile. As shown in figure 26, the magnitude and temporal fluctuation of C_F decrease as *AR* increases. For *AR* 1, the body with a rough surface has a smaller C_F (i.e. reduced drag) at $t^* \lesssim 14$ and $t^* \lesssim 17$ at $U_\circ = 2.5$ m s^{-1} and 4.2 m s^{-1}, respectively. After cavity pinch-off, C_F starts to decrease in both cases and that of the smooth surface shows larger oscillation. At this stage, the body with a smooth surface has a smaller C_F and even has negative values at $22 \lesssim t^* \lesssim 40$ and $25 \lesssim t^* \lesssim 45$ for $U_\circ = 2.5$ m s^{-1} and 4.2 m s^{-1}, respectively. The same trend of C_F for an underwater sinking body was previously reported by Truscott *et al.* (2012). As mentioned earlier, the projectile is locally accelerated by the shed vortices in the wake. After this unstable stage, C_F increases and approaches zero as terminal velocity is reached. For a rough sphere, this wake-induced instability is delayed (or reduced) due to the cavity and thus C_F saturates faster than it does for a smooth sphere. When $AR = 2.0$, the rough body has a slightly larger (or similar) C_F than the smooth one due to the increased pressure drag caused by the air bubbles attached to the body after pinch-off. For *AR* 4, the delayed rotation of a body with a rough surface results in a smaller C_F. Lastly, for *AR* 8, both the smooth and rough bodies exhibit C_F values of almost zero. With the present set-up, it is not possible to distinguish differences in the sinking dynamics of projectiles with higher *AR* ($\gtrsim 8.0$), but it would be interesting to work with a larger water tank to investigate these features further.

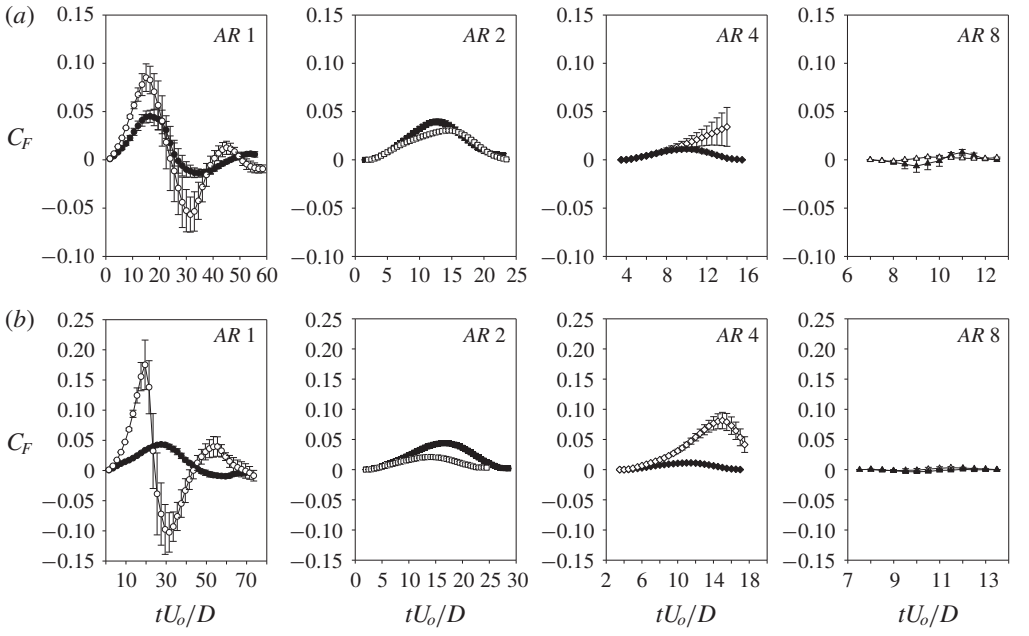

FIGURE 26. Temporal variation of C_F: (*a*) $U_\circ = 2.5$ m s^{-1}; (*b*) 4.2 m s^{-1}. The open and closed symbols correspond to smooth and rough surfaces, respectively. Positive values of C_F correspond to the upward direction (i.e. drag force on a sinking body).

6. Concluding remarks

In the present study, we experimentally investigated the formation and evolution of jets, splashes and underwater cavities following the water entry of rounded cylindrical bodies while varying aspect ratio as well as the surface conditions and impact speeds of the bodies. The surface condition of the front part governs the global picture of the subsequent phenomena. When it is smooth, the water layer displaced from the projectile rises along the surface of the projectile without separation. Depending on the aspect ratio, the water film may converge at the rear pole to create a jet or simply moves up and down the surface of the falling body. In addition to the apex jet (which we call a thin jet), the stagnation pressure right below the free surface due to the wake behind a body causes the rise of another jet, a thick jet. It was also found that the balance between the viscous force and surface tension determines the conditions under which jet-tip breakdown occurs. On the other hand, the impact speed (within the considered range) does not influence the jet dynamics significantly.

When the front part of a projectile is rough, the water film rise cannot be retained for long and early separation occurs. This behaviour produces a splash and cavity above and below the free surface, respectively. Due to the imbalance of the surrounding forces, the splash shrinks into a dome and cavity pinch-off occurs, but the projectile strongly interferes with this process as aspect ratio increases. The effect of an underwater cavity on the hydrodynamic force on a sinking body shows quite interesting dependencies on the body aspect ratio and impact speed. If the aspect ratio is small and the inertia is sufficiently strong, then a stably formed (i.e. axisymmetric) cavity fully covers the body, forming a boundary between the solid body and surrounding water. In this case, the cavity reduces the drag force on the

body. However, if the cavity is unstable due to the reduced inertia or the cavity bubbles partially attach to the body surface after pinch-off, the drag force increases. The drag reduction on the well-defined outer profile of an underwater cavity was recently addressed by Vakarelski *et al.* (2017).

While we focused on the time immediately after impact, e.g. from jet (splash) formation to cavity pinch-off, the wake-induced path instability of a sinking body was also briefly introduced. Furthermore, we demonstrated that this instability is delayed due to cavity formation, which eventually affects the dynamics of a sinking body. It would be interesting to focus on the time ranges when this wake instability starts to appear and to investigate the influence of a cavity. In addition, the detailed mechanism of (or conditions necessary for) early separation of a water film from an impacting body with a rough surface remains to be uncovered. We are currently working on these issues to further our understanding of the water entry problem.

Acknowledgements

This work was supported by a grant (KCG-01-2017-02) through the Disaster and Safety Management Institute and grants (2016R1C1B2012775, 2017R1A4A1015523, 2017M2A8A4018482) through the National Research Foundation (NRF) of Korea, funded by the Korean government (KCG and MSIP, respectively) via SNU-IAMD.

Supplementary movies

Supplementary movies are available at https://doi.org/10.1017/jfm.2018.1026.

REFERENCES

AGÜÍ, J. C. & JIMÉNEZ, J. 1987 On the performance of particle tracking. *J. Fluid Mech.* **185**, 447–468.

ARISTOFF, J. M. & BUSH, J. W. M. 2009 Water entry of small hydrophobic spheres. *J. Fluid Mech.* **619**, 45–78.

ARISTOFF, J. M., TRUSCOTT, T., TECHET, A. H. & BUSH, J. W. M. 2010 The water entry of decelerating spheres. *Phys. Fluids* **22**, 032102.

BENKREIRA, H. & KHAN, M. I. 2008 Air entrainment in dip coating under reduced air pressures. *Chem. Engng Sci.* **63**, 448–459.

BODILY, K. G., CARLSON, S. J. & TRUSCOTT, T. T. 2014 The water entry of slender axisymmetric bodies. *Phys. Fluids* **26**, 072108.

CHEN, R. C., YU, Y. T., SU, K. W., CHEN, J. F. & CHEN, Y. F. 2013 Exploration of water jet generated by Q-switched laser induced water breakdown with different depths beneath a flat free surface. *Opt. Express* **21**, 445–453.

CLANET, C., HERSEN, F. & BOCQUET, L. 2004 Secrets of successful stone-skipping. *Nature* **427**, 29.

COX, R. G. 1986 The dynamics of the spreading of liquids on a solid surface. *J. Fluid Mech.* **168**, 169–194.

DAS, S., CHANDA, S., EIJKEL, J. C. T., TAS, N. R., CHAKRABORTY, S. & MITRA, S. K. 2014 Filling of charged cylindrical capillaries. *Phy. Rev.* E **90**, 043011.

DRIESSEN, T., JEURISSEN, R., WIJSHOFF, H., TOSCHI, F. & LOHSE, D. 2013 Stability of viscous long liquid filaments. *Phy. Fluids* **25**, 062109.

DUCLAUX, V., CAILLE, F., DUEZ, C., YBERT, C., BOCQUET, L. & CLANET, C. 2007 Dynamics of transient cavities. *J. Fluid Mech.* **591**, 1–19.

DUEZ, C., YBERT, C., CLANET, C. & BOCQUET, L. 2007 Making a splash with water repellency. *Nat. Phys.* **3**, 180–183.

DUSSAN, E. B. V. 1979 On the spreading of liquids on solid surfaces: static and dynamic contact lines. *Annu. Rev. Fluid Mech.* **11**, 371–400.

EGGERS, J. & VILLERMAUX, E. 2008 Physics of liquid jets. *Rep. Prog. Phys.* **71**, 036601.

ERN, P., RISSO, F., FABRE, D. & MAGNAUDET, J. 2012 Wake-induced oscillatory paths of bodies freely rising or falling in fluids. *Annu. Rev. Fluid Mech.* **44**, 97–121.

GEKLE, S., VAN DER BOS, A., BERGMANN, R., VAN DER MEER, D. & LOHSE, D. 2008 Noncontinuous Froude number scaling for the closure depth of a cylindrical cavity. *Phys. Rev. Lett.* **100**, 084502.

GRUMSTRUP, T., KELLER, J. B. & BELMONTE, A. 2007 Cavity ripples observed during the impact of solid objects into liquids. *Phys. Rev. Lett.* **99**, 114502.

HARRISON, S. M., COHEN, R. C., CLEARY, P. W., BARRIS, S. & ROSE, G. 2016 A coupled biomechanical-smoothed particle hydrodynamics model for predicting the loading on the body during elite platform diving. *Appl. Math. Model.* **40**, 3812–3831.

KUBIAK, K. J., WILSON, M. C. T., MATHIA, T. G. & CARVAL, P. 2011 Wettability versus roughness of engineering surfaces. *Wear* **271**, 523–528.

KUBOTA, Y. & MOCHIZUKI, O. 2009 Splash formation by a spherical body plunging into water. *J. Vis.* **12**, 339–346.

KUBOTA, Y. & MOCHIZUKI, O. 2011 Influence of head shape of solid body plunging into water on splash formation. *J. Vis.* **14**, 111–119.

KUWABARA, G., TANBA, H. & KONO, K. 1987 Splash produced by a smooth sphere or circular cylinder striking a liquid surface. *J. Phys. Soc. Japan* **56**, 2733–2743.

LANDRETH, C. C. & ADRIAN, R. J. 1990 Impingement of a low Reynolds number turbulent circular jet onto a flat plate at normal incidence. *Exp. Fluids* **9**, 74–84.

LATKA, A., STRANDBURG-PESHKIN, A., DRISCOLL, M. M., STEVENS, C. S. & NAGEL, S. R. 2012 Creation of prompt and thin-sheet splashing by varying surface roughness or increasing air pressure. *Phys. Rev. Lett.* **109**, 054501.

LEE, M., LONGORIA, R. G. & WILSON, D. E. 1997 Cavity dynamics in high-speed water entry. *Phys. Fluids* **9**, 540–550.

MANSOOR, M. M., MARSTON, J. O., VAKARELSKI, I. U. & THORODDSEN, S. T. 2014 Water entry without surface seal: extended cavity formation. *J. Fluid Mech.* **743**, 295–326.

MANSOOR, M. M., VAKARELSKI, I. U., MARSTON, J. O., TRUSCOTT, T. T. & THORODDSEN, S. T. 2017 Stable-streamlined and helical cavities following the impact of Leidenfrost spheres. *J. Fluid Mech.* **823**, 716–754.

MARSTON, J. O., SEVILLE, J. P. K., CHEUN, Y.-V., INGRAM, A., DECENT, S. P. & SIMMONS, M. J. H. 2008 Effect of packing fraction on granular jetting from solid sphere entry into aerated and fluidized beds. *Phys. Fluids* **20**, 023301.

MARSTON, J. O. & THORODDSEN, S. T. 2008 Apex jets from impacting drops. *J. Fluid Mech.* **614**, 293–302.

MARSTON, J. O., TRUSCOTT, T. T., SPEIRS, N. B., MANSOOR, M. M. & THORODDSEN, S. T. 2016 Crown sealing and buckling instability during water entry of spheres. *J. Fluid Mech.* **794**, 506–529.

MARSTON, J. O., VAKARELSKI, I. U. & THORODDSEN, S. T. 2011 Bubble entrapment during sphere impact onto quiescent liquid surfaces. *J. Fluid Mech.* **680**, 660–670.

MAY, A. 1951 Effect of surface condition of a sphere on its water-entry cavity. *J. Appl. Phys.* **22**, 1219–1222.

MAY, A. 1952 Vertical entry of missiles into water. *J. Appl. Phys.* **23**, 1362–1372.

NOTZ, P. K. & BASARAN, O. A. 2004 Dynamics and breakup of a contracting liquid filament. *J. Fluid Mech.* **512**, 223–256.

OTSU, N. 1979 A threshold selection method from gray-level histograms. *IEEE Trans. Syst. Man Cybern.* **9**, 62–66.

PLATEAU, J. 1873 *Experimental and Theoretical Steady State of Liquids Subjected to Nothing but Molecular Forces*. Gauthiers-Villars.

RAYLEIGH, F. 1878 On the instability of jets. *Proc. Lond. Math. Soc.* **5**, s1–10.

ROSELLINI, L., HERSEN, F., CLANET, C. & BOCQUET, L. 2005 Skipping stones. *J. Fluid Mech.* **543**, 137–146.

ROYER, J. R., CORWIN, E. I., CONYERS, B., FLIOR, A., RIVERS, M. L., ENG, P. J. & JAEGER, H. M. 2008 Birth and growth of a granular jet. *Phys. Rev.* E **78**, 011305.

SHEPARD, T., ABRAHAM, J., SCHWALBACH, D., KANE, S., SIGLIN, D. & HARRINGTON, T. 2014 Velocity and density effect on impact force during water entry of sphere. *J. Geophys. Remote Sens.* **3**, 129.

STONE, H. A., BENTLEY, B. J. & LEAL, L. G. 1986 An experimental study of transient effects in the breakup of viscous drops. *J. Fluid Mech.* **173**, 131–158.

SUN, H. & FALTINSEN, O. M. 2006 Water impact of horizontal circular cylinders and cylindrical shells. *Appl. Ocean Res.* **28**, 299–311.

THORODDSEN, S. T., ETOH, T. G., TAKEHARA, K. & TAKANO, Y. 2004 Impact jetting by a solid sphere. *J. Fluid Mech.* **499**, 139–148.

TRUSCOTT, T. T., EPPS, B. P. & BELDEN, J. 2014 Water entry of projectiles. *Annu. Rev. Fluid Mech.* **46**, 355–378.

TRUSCOTT, T. T., EPPS, B. P. & TECHET, A. H. 2012 Unsteady forces on spheres during free-surface water entry. *J. Fluid Mech.* **704**, 173–210.

VAKARELSKI, I. U., KLASEBOER, E., JETLY, A., MANSOOR, M. M., AGUIRRE-PABLO, A. A., CHAN, D. Y. C. & THORODDSEN, S. T. 2017 Self-determined shapes and velocities of giant near-zero drag gas cavities. *Sci. Adv.* **3**, e1701558.

WORTHINGTON, A. M. 1908 *A Study of Splashes*. Longmans.

YAO, E., WANG, H., PAN, L., WANG, X. & WODING, R. 2014 Vertical water-entry of bullet-shaped projectiles. *J. Appl. Math. Phys.* **2**, 323–334.

ZHAO, M. H., CHEN, X. P. & WANG, Q. 2014 Wetting failure of hydrophilic surfaces promoted by surface roughness. *Sci. Rep.* **4**, 5376.

ZHAO, R. & FALTINSEN, O. 1993 Water entry of two-dimensional bodies. *J. Fluid Mech.* **246**, 593–612.